Trends and variability of polar mesopause region temperatures attributed to atmospheric dynamics and solar activity

—

Silje Eriksen Holmen
A dissertation for the degree of Philosophiae Doctor – October 2016

Front page image:
Airglow and a meteor penetrating Earth's atmosphere, photographed at night over Irkutsk, Russia, from the International Space Station on 13 August 2011.
NASA Earth Observatory, http://earthobservatory.nasa.gov/IOTD/view.php?id=51754

Abstract

The mesopause region can be considered a "boundary region" between the neutral atmosphere, where atmospheric constituents and momentum are transported mainly by winds and turbulent eddies, and the ionosphere, where the main transport mechanism is molecular diffusion. In the mesopause, complex interactions between dynamics and photochemistry occur, and we are far from a complete understanding of these interactions.

This thesis aims to better understand the processes responsible for the large temperature fluctuations we observe in the polar mesopause region, especially the effects of atmospheric circulation and wave activity from lower atmospheric layers. Investigations of trends have also been conducted. To carry out these investigations, we have derived and examined mesopause temperatures from two high-latitude locations: Tromsø (70°N, 19°E) and Longyearbyen (78°N, 16°E), and turbopause height only from Tromsø. A long-term change in turbopause height may be important for understanding processes that are responsible for redistribution of atmospheric constituents.

We examined winter season variations in the hydroxyl (OH*) airglow temperature record from Longyearbyen and identified local temperature maxima in mid-January and mid-February, as well as a minimum in the transition between December and January. We also identified a number of statistically significant periodic oscillations in temperatures derived from the Nippon/Norway Tromsø Meteor Radar, with periods ranging from 9 days to a year. The seasonal variation showed higher temperatures and variability during winter compared to summer. We also found local temperature enhancements just after spring equinox and summer solstice. Temperature variability and seasonal variation may, to a large extent, be explained by the large-scale circulation in the middle atmosphere and corresponding wave activity.

The trends for the Longyearbyen OH* airglow winter temperature series and meteor radar derived temperatures from Tromsø, both annual and summer trends, were estimated to be near-zero or slightly negative. The Tromsø winter trend was negative, $(-11.6 \pm 4.1)\,\mathrm{K\,decade^{-1}}$.

We derived turbopause altitude from turbulent energy dissipation rates obtained from the Tromsø medium-frequency radar and found an increasing height in summer, $(1.6 \pm 0.3)\,\mathrm{km\,decade^{-1}}$, during the time period from 2002 until 2015, while in winter turbopause height did not change significantly. We investigated the response of the change in turbopause height to a change in

temperature, but a changing temperature did not alter trends significantly, irrespective of season.

Preface

This thesis is submitted for the degree of Philosophiae Doctor (PhD) at the University of Tromsø (UiT) - The Arctic University of Norway. The work and research described herein were conducted at the University Centre in Svalbard (UNIS) and funded through their grant from the Norwegian Ministry of Education and Research. The research in this thesis has been conducted as a part of the Birkeland Centre for Space Science (BCSS), a cooperative effort between the University of Bergen, Norwegian University of Science and Technology and UNIS.

The thesis consists of an introductory part and four papers, published in peer-reviewed journals. Below is a list of the papers, including the contributions of authors.

Paper 1
Holmen, S. E., M. E. Dyrland, and F. Sigernes (2013), Mesospheric temperatures derived from three decades of hydroxyl airglow measurements from Longyearbyen, Svalbard (78°N), *Acta Geophysica*, 62 (2), 302–315,
doi: 10.2478/s11600-013-0159-4.

S.E.H. performed the data analyses and wrote the paper. M.E.D. and F.S. took part in discussions and contributed with helpful comments.

Paper 2
Holmen, S. E., M. E. Dyrland, and F. Sigernes (2014), Long-term trends and the effect of solar cycle variations on mesospheric winter temperatures over Longyearbyen, Svalbard (78°N), *Journal of Geophysical Research: Atmospheres*, 119, 6596–6608, doi: 10.1002/2013JD021195.

S.E.H. performed the data analyses and wrote most of the paper. M.E.D. and F.S. contributed with comments to the draft and wrote parts of the sections involving calibration, measurement technique and discussion regarding the height of the OH* layer and corresponding implications for temperature.

Paper 3
Hall, C. M., S. E. Holmen, C. E. Meek, A. H. Manson, and S. Nozawa (2016), Change in turbopause altitude at 52 and 70°N, *Atmospheric Chemistry and*

Physics, 16, 2299–2308, doi: 10.5194/acp-16-2299-2016.

C.M.H. did most of the data analyses and wrote the paper. S.E.H. contributed with temperature trend assessment and took part in discussions and gave feedback on the manuscript draft. C.E.M., A.H.M. and S.N. took part in discussions and gave feedback on the draft.

Paper 4

Holmen, S. E., C. M. Hall, and M. Tsutsumi (2016), Neutral atmosphere temperature change at 90 km, 70°N, 19°E, 2003–2014, *Atmospheric Chemistry and Physics*, 16, 7853–7866, doi: 10.5194/acp-16-7853-2016.

S.E.H. did the data analyses and wrote the paper. C.M.H. and M.T. took part in discussions and gave feedback on the draft.

Acknowledgements

Contents

Contents

1. Introduction

1.1. Earth's atmosphere

Earth's atmosphere can be divided into different layers according to its characteristics at different altitudes. One way of classifying the atmosphere is in terms of temperature, see Figure 1.1. The *troposphere* is the lowest layer of the atmosphere, and most weather phenomena are confined within this layer. Tropospheric air is heated, or on occasion cooled, at the surface and through conduction and convection. Temperature decreases with increasing altitude as pressure decreases, following the adiabatic lapse rate. The stratosphere and mesosphere are commonly referred to as the *middle atmosphere*. The *stratosphere* extends from about 10 km (over polar regions) to about 50 km altitude, and temperature here increases with height due to the absorption of ultraviolet (UV) radiation by ozone. The region from about 50 km to about 100 km is called the *mesosphere*. Here temperature decreases with increasing altitude and follows the adiabatic lapse rate again, due to that heating by UV absorption by ozone falls off. Carbon dioxide has a cooling effect here by radiating heat into space, as opposed to further down in the atmosphere, where it acts as a greenhouse gas by absorbing infrared radiation emitted from Earth's surface. The upper-most part of the mesosphere is the *mesopause*, which is the coldest region of the atmosphere. The *thermosphere* is located directly above the mesopause and is the lowest layer of the upper atmosphere. High-energy X-rays and UV radiation from the Sun are absorbed in this layer, raising its temperature to hundreds or sometimes more than 1000 K, depending on solar activity. The mesosphere and lower thermosphere are often considered a distinct atmospheric region, commonly abbreviated the *MLT region*, because the two share some common dynamic features. Gravity waves generated in the lower atmosphere propagate upwards and break in this region, influencing the mean circulation and thermal structure of the middle atmosphere.

The atmosphere can also be divided into two layers depending on the nature of atmospheric mixing: the homosphere and the heterosphere. The *homosphere* is the part of the atmosphere below about 90 km to 100 km, depending on season, where atmospheric mixing is dominated by turbulence. The *heterosphere* is located above the homosphere. Here, molecular diffusion dominates over eddy mixing so that constituents become separated vertically according to their molecular masses. The demarcation between the two layers is called
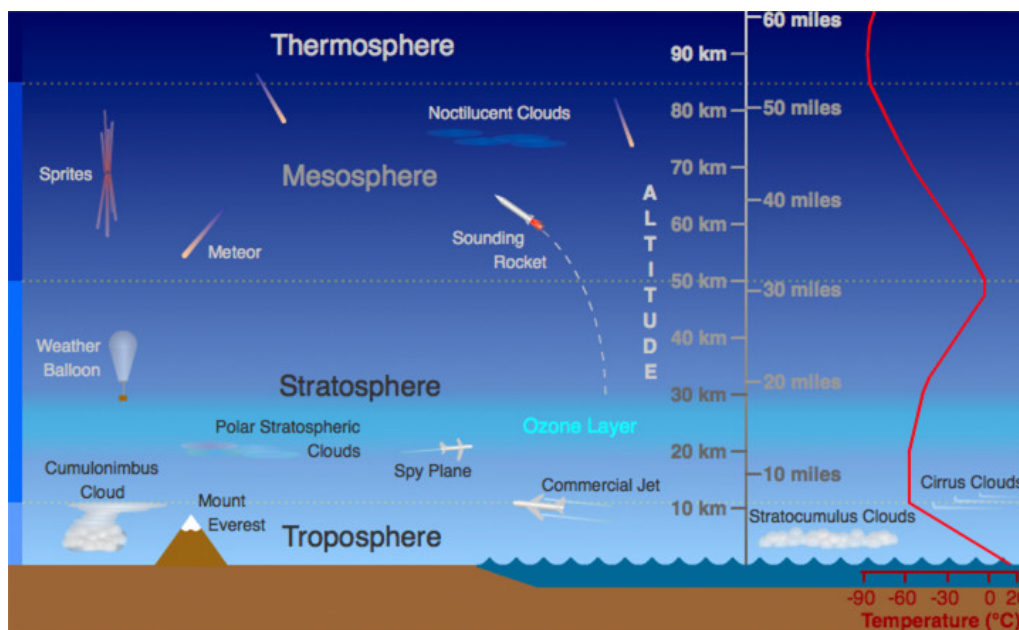
Figure 1.1.: Structure of Earth's atmosphere up to 100 km altitude. Image credit: Randy Russell, UCAR.

the *turbopause* or the *homopause*. The higher the altitude of the turbopause, the greater the downward mixing of products of photochemical processes, and the more effective the upward transport of trace gases out of the underlying regions into the upper atmosphere.

A third way of classifying the atmosphere is in terms of ionisation. The *neutral atmosphere* consists of neutral atoms and molecules, in contrast to the *ionosphere*, where gas molecules are ionised, which means that they carry an electric charge by gaining or losing electrons with the aid of high-energy solar radiation. The ionosphere is not a distinct atmospheric layer, but rather a series of regions located in parts of the mesosphere and thermosphere. The ionospheric regions are called the *D, E and F layers*, or regions, where the D layer is the lowest layer.

1.2. Why and how study the mesopause region?

The atmospheric region of interest in this thesis is the mesopause region. At first glance, one can wonder about the importance of studying the mesopause. It is located far away from where we live, and to our knowledge there are no processes going on there that are threatening human life or life quality, as opposed to ozone layer depletion in the stratosphere or hurricanes in the troposphere. Research involving the mesopause region is therefore to some extent fundamental research. However, it can be applied research as well.

The mesopause can be considered a "boundary region" between the neutral atmosphere and the ionosphere. In the neutral atmosphere, the main transport mechanism is transport by winds and turbulent eddies. In the ionosphere, the main transport mechanism is molecular diffusion, which describes fluxes of atoms and molecules from a region of higher concentration to one of lower concentration. The ionised constituents of the ionosphere are governed by physical laws that differ substantially from the laws governing neutral gases. In the mesopause region, we have complex interactions between dynamics, photochemistry and heating, and we are far from a complete understanding of these interactions.

The mesopause is one of the most poorly understood layers of the atmosphere. This is mainly because it is difficult to make direct measurements of basic atmospheric parameters like temperature and wind velocity here. Weather balloons and aircraft do not reach higher up than the stratosphere, and satellites orbit above the mesopause region and can only give indirect inferences of temperature and wind speed of this region. Sounding rockets make measurements in situ, but they are expensive and only give short, infrequent glimpses of the state of the atmosphere. The processes occurring in the mesopause are therefore not easily measured. However, some interesting phenomena occur in the mesopause, which we can utilise to derive key parameters of the region. Examples of such phenomena are airglow, polar mesospheric clouds/summer echoes and meteor ablation.

Airglow is the collective term for light emissions from excited atoms and molecules located approximately between 80 km and 100 km altitude in the atmosphere. The atoms and molecules are excited by the Sun's extreme ultraviolet (EUV) radiation and recombined to produce light emissions. From intensities of airglow emissions, we are able to determine temperatures in the mesopause region (e.g. French et al., 2000; Mies, 1974; Sigernes et al., 2003). Gravity waves and planetary waves, originating from the troposphere and stratosphere, modulate atmospheric density, temperature and composition, as well as airglow intensity. Thus, airglow emissions can be utilised for observing structures from waves propagating from the lower atmosphere, and hence for investigating atmospheric coupling (e.g. Viereck and Deehr, 1989).

The very low temperatures in the summer mesopause allow ice particles to form and grow. The largest ice particles develop into polar mesospheric clouds (PMC), which are tenuous clouds extending poleward of 50° in both hemispheres during summer. PMC are not visible from the ground poleward of 65° due to the light conditions during the Arctic and Antarctic summers (Olivero and Thomas, 1986). They require low solar elevation illumination from an observer's point of view in order to be detected. The smallest ice particles are associated with strong radar echoes, known as polar mesosphere summer echoes (PMSE). The ice particles are charged by plasma of the D

region of the ionosphere and transported by the turbulent velocity field, leading to small-scale structures in the spatial distribution of the electron number density. The resulting occurrence of irregularities in the radio refractive index is observed by radars on the ground as PMSE (Czechowsky et al., 1988; Ecklund and Balsley, 1981; Hoppe et al., 1988). PMSE give insight to key atmospheric parameters like neutral temperatures, winds, gravity waves and turbulence (Rapp and Lübken, 2004; Röttger et al., 1988). PMSE are not investigated in this PhD project.

Meteoroids frequently enter Earth's atmosphere where they are slowed down by friction with atmospheric atoms and molecules in the MLT region. The kinetic energy of a meteoroid is converted into heat, sufficient to sublime and ionise the surface of the meteoroid and to ionise the atoms and molecules of the surrounding atmosphere. The resulting plasma trail can be utilised to determine neutral temperatures and wind velocities in the region (McKinley, 1961).

In addition to the phenomena described above, we can get inferred mesospheric temperatures and wind speeds from satellite measurements. Even though satellites cannot measure temperature directly, they can measure radiance given off by atmospheric constituents, whose intensities are proportional to air temperature (e.g. Waters et al., 2006). Wind speeds can be derived using interferometry of Doppler-shifted optical spectra (Pierce and Roark, 2012).

1.3. Motivation and structure of this thesis

In the previous section, general motivation for studying the mesopause region was exhibited. The motivation for this PhD project can be divided into two main objectives. The first objective is to gain further knowledge of processes responsible for circulation and other dynamic features in the polar mesopause region, especially the effects of wave activity from lower atmospheric layers on mesopause region temperatures. Temperatures in the mesopause region are highly variable. Sometimes they can vary by $30\,\mathrm{K}$ to $50\,\mathrm{K}$ within just a few days, as can be seen in Figure 1.2. This figure shows temperatures derived from airglow over Longyearbyen in late January and early February 2012. The mechanisms behind this large variability are not completely understood. Understanding dynamical, radiative and chemical couplings between different atmospheric layers are crucial in order to assess temperature changes in the mesopause region. This thesis aims to better understand the processes responsible for the temperature fluctuations we observe.

The second objective is to investigate trends in polar mesopause region temperature and turbopause height. It has been generally accepted for decades that increasing anthropogenic emissions of greenhouse gases are responsible
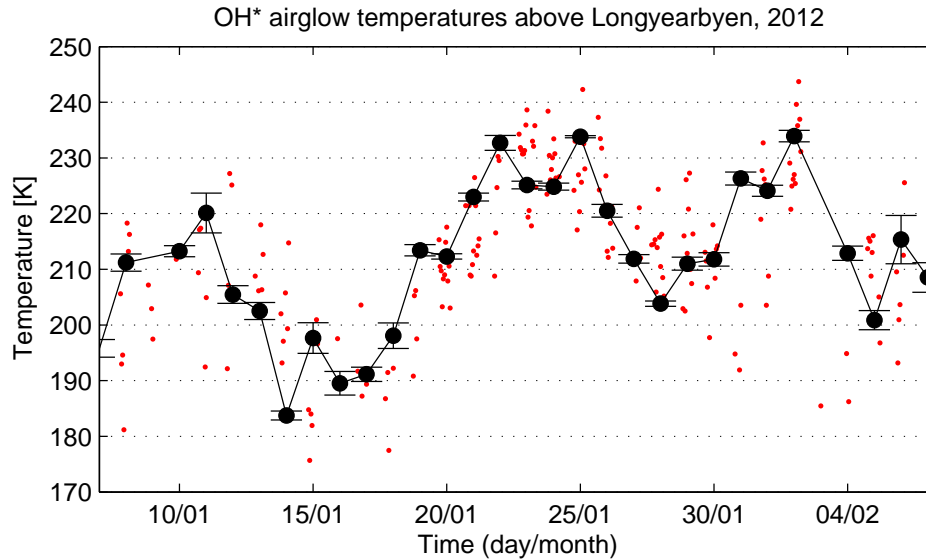
Figure 1.2.: Mesopause temperatures estimated from airglow intensities measured by the 1m Ebert-Fastie spectrometer located at the Kjell Henriksen Observatory in Longyearbyen in 2012. Red dots are hourly temperatures. Black bullets are daily averages. Error bars represent weighted uncertainties of daily temperatures.

for warming of the lower atmosphere (e.g. Manabe and Wetherald, 1975). These emissions are proposed to cause the mesosphere and thermosphere to cool (Akmaev and Fomichev, 2000; Roble and Dickinson, 1989). Akmaev and Fomichev (1998) report, using a middle atmospheric model, that if CO_2 concentrations are doubled, temperature will decrease by about $10\,\mathrm{K}$ in the upper mesosphere. Newer and more sophisticated models include important radiative and dynamical processes as well as interactive chemistries, and results from these models show a cooling of $3\,\mathrm{K}$ to $5\,\mathrm{K}$ in the high-latitude winter mesopause and insignificant or even a slight warming in the high-latitude summer mesopause (e.g. Fomichev et al., 2007; Schmidt et al., 2006). Observational studies on long-term trends of mesopause region temperatures from mid-latitude and high-latitude sites report slightly negative or near-zero trends (e.g. French and Klekociuk, 2011; Offermann et al., 2010). The complexity of temperature trends in the mesopause region and their causes act as motivation for studying this matter further. Investigating a long-term change in turbopause height may give insight to processes that are responsible for redistribution of atmospheric constituents.

To investigate the two main objectives of this thesis, we have utilised temperatures from two high-latitude locations, derived from hydroxyl (OH*) airglow and meteor radar, as well as estimates of turbopause height. Figure A.1 in the Appendix shows the two locations: Tromsø (70°N, 19°E) in Northern

5

Norway and Longyearbyen (78°N, 16°E) in the Svalbard archipelago.

The structure of this PhD thesis is as follows. Chapter 2 addresses underlying background for the results presented. In Chapter 3, theory behind hydroxyl airglow spectra and the chemistry of the hydroxyl airglow layer are described. The process of retrieving rotational temperatures from airglow intensities is also described. The theory behind retrieval of mesospheric temperatures from meteor radar, together with turbopause height derived from medium-frequency radar are treated in Chapter 4. In Chapter 5, main results are presented and discussed. Concluding remarks are given in Chapter 6, and perspectives for the future are given in Chapter 7. The papers published as a part of this PhD thesis are listed at the end.

2. Processes influencing the middle atmosphere

This chapter aims to cover background theory necessary for understanding the main results obtained in this PhD project. In Section 2.1, observed zonal winds and temperatures in the middle atmosphere are presented, together with general circulation patterns. Section 2.2 briefly describes waves responsible for driving the atmospheric circulation. Section 2.3 treats sudden stratospheric warmings, which are events that are triggered by these waves and that act as a coupling mechanism in the middle atmosphere. Section 2.4 gives a short introduction to some basic characteristics of turbulence necessary for understanding the derivation of turbopause height, which will be presented in Chapter 4. In Section 2.5, effects of solar forcing on mesopause region temperature are presented. Finally, Section 2.6 briefly describes other influences on circulation and chemistry of the middle atmosphere.

2.1. Temperature distribution and circulation

If turbulence is disregarded, the middle atmosphere would be in approximate radiative equilibrium (e.g. Fels, 1985). The temperature distribution would show a strong seasonal dependence with maximum temperature at the stratospheric summer pole and minimum at the mesospheric winter pole, see Figure 2.1. However, reality tells a different story.

Cross sections of observed zonal mean temperature in the atmosphere up to 80 km for January and July are shown in the top left and right panels of Figure 2.2, respectively. In the stratosphere, infrared radiative cooling is balanced primarily by radiative heating due to absorption of solar UV radiation by ozone. We see that mean temperature increases with height until a maximum is reached at the stratopause near 50 km. Above the stratopause, the temperature gradient gradually resumes the adiabatic lapse rate as the ozone concentration falls off with height. Minimum temperature is reached over the summer pole at the mesopause.

If we compare observed temperature with "radiatively" determined temperature for January, we see that the summer polar stratosphere is under strong radiative control, but over the winter stratosphere and mesosphere observed temperature is 60 K to 100 K higher than temperature estimated based only

January Radiatively Determined Temperature
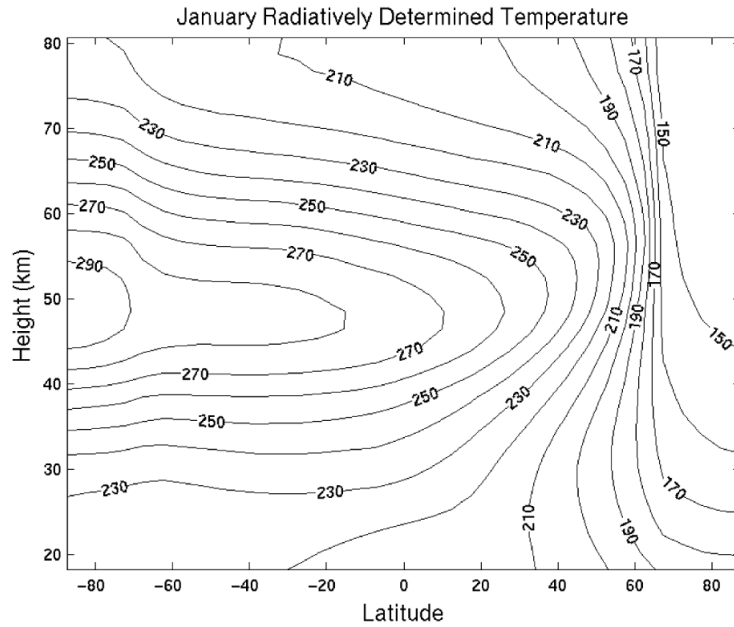
Figure 2.1.: Temperature distribution [K] in the middle atmosphere for Northern winter solstice expected for an atmosphere in radiative equilibrium. From Holton (2004), based on Shine (1987).

on radiative balance. Obviously, temperatures in the middle atmosphere are not determined by radiation alone. Dynamics and transport largely influence both the temperature distribution and the composition of the middle atmosphere (Andrews et al., 1987; Fritts and Alexander, 2003).

The two bottom panels of Figure 2.2 show cross sections of observed monthly zonal wind for January and July. The main features are a westward jet in the summer hemisphere and an eastward jet in the winter hemisphere, with maximum wind speeds reached near 60 km.

The atmosphere is a complex system which allows transport of momentum, heat, particles and compounds from one layer to another. Waves propagating from lower layers of the atmosphere and dissipating momentum into the MLT region drive the mean circulation to a large extent (e.g. Garcia and Solomon, 1985). This residual circulation is shown in Figure 2.3 and is characterised by rising motions above 30 km in the summer hemisphere, with flow from the summer to the winter hemisphere in the upper stratosphere and mesosphere, and descent in the winter hemisphere (Dunkerton, 1978; Murgatroyd and Singleton, 1961). Downwelling of air over the winter pole causes the air to be compressed and adiabatically heated. Conversely, upwelling at the summer pole causes air to expand, leading to a cooling of the summer mesopause. Therefore, the summer mesopause is cooler than the winter mesopause. The lower stratospheric part of the circulation is called the Brewer-Dobson cir-

Figure 2.2.: Observed monthly and averaged temperature [K] and zonal wind [m/s] for January (left) and July (right). Negative wind speeds (dotted contours) represent westward (easterly, from east) winds, while positive wind speeds (solid line contours) represent eastward (westerly, from west) winds. From Holton (2004), based on Fleming et al. (1990).

culation and consists of rising motions at low latitudes and descent at high latitudes, approximately symmetric about the equator (Brewer, 1949; Dobson, 1956).

2.2. Planetary waves and gravity waves

Two groups of waves largely responsible for driving the atmospheric circulation are gravity waves (GWs) and planetary waves (PWs). GWs are created in the troposphere, e.g. by thunderstorm updrafts, Kelvin-Helmholtz instability around the jet stream or when winds flow over mountains (orographic forcing). Their restoring force is buoyancy. They can propagate vertically and horizontally, and both eastwards and westwards, but only against the zonal flow, or if they have higher phase speeds than the background flow. During westward zonal flow, westward-propagating GWs are filtered out at a so-called critical layer and vice versa. A critical layer is reached where the phase velocity of the wave is equal to the mean fluid velocity, and momentum
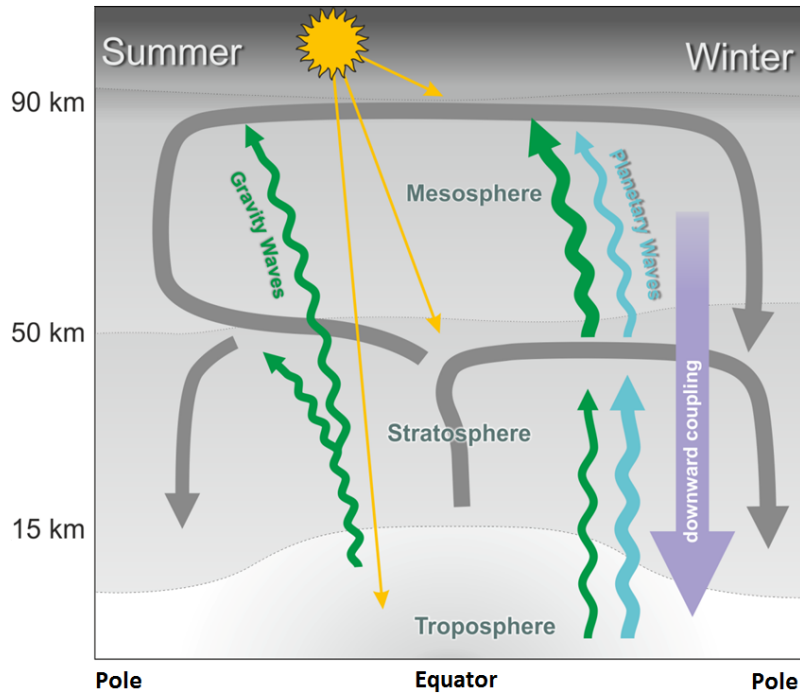
Figure 2.3.: Schematic representation of the residual circulation of the middle atmosphere. The stratospheric part of the circulation is called the Brewer-Dobson circulation. The mesospheric part is commonly referred to as the mesospheric residual circulation. Image credit: Jülich Forschungszentrum.

is transferred to the mean flow (Booker and Bretherton, 1967). During winter, when the mean stratospheric zonal flow is eastward, only GWs with westward phase speeds can propagate vertically. During equinox, stratospheric winds reverse, and the dominant direction of GWs in the mesosphere also reverses. During summer, the mean stratospheric zonal flow is westward, and therefore only GWs with eastward phase speeds can propagate vertically.

GWs in the upper mesosphere typically have vertical wavelengths ranging from 2 km to 30 km, periods of a few minutes to a few hours and horizontal phase speeds of up to $80 \, \text{m s}^{-1}$ (Andrews et al., 1987; Fritts, 1984; Hines, 1960).

Planetary waves, or Rossby waves, are caused by meridional perturbations of the zonal flow (Rossby, 1939). The waves with the largest amplitudes arise when the atmosphere in motion encounters changing surfaces, e.g. large-scale orography or land-sea contrasts, and is forced to ascend, due to a changing surface topography, and descend, due to gravity. Their restoring force is provided by the latitudinal gradient of the planetary vorticity caused by Earth's rotation. Potential vorticity must be conserved, resulting in that air that is forced to ascend tends to turn to the left, and as it descends again it turns to
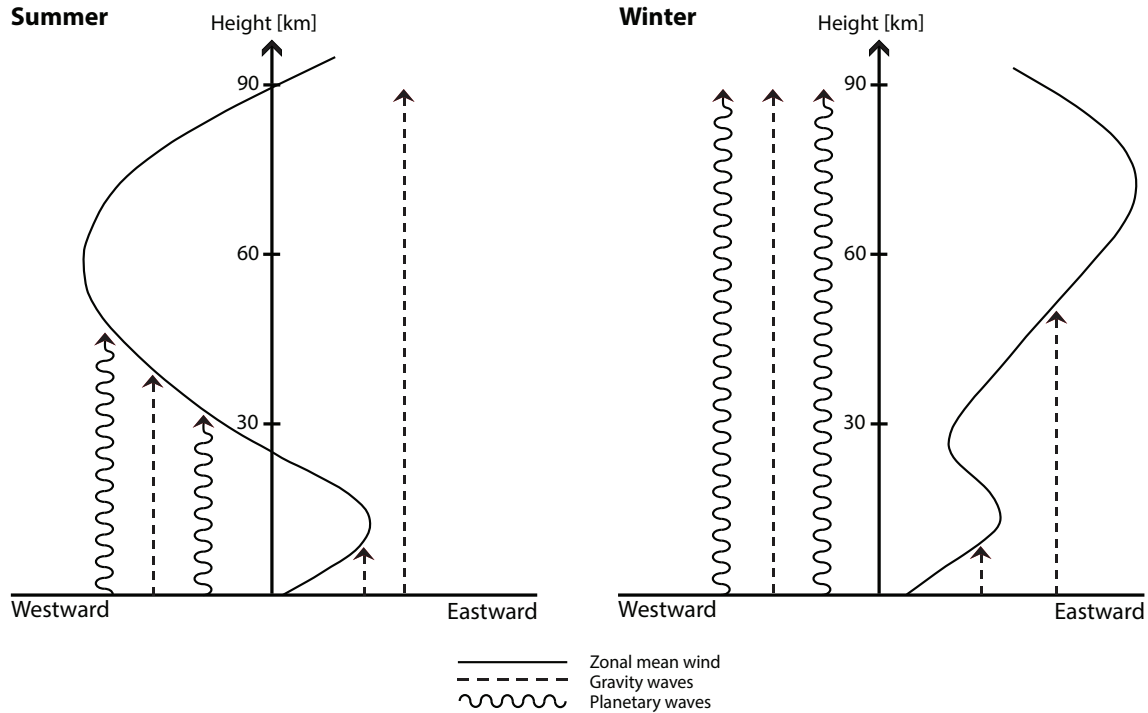
Figure 2.4.: Propagation of gravity waves and planetary waves during Northern Hemisphere summer (left) and winter (right).

the right (Dickinson, 1978).

PWs can only propagate westwards. If the zonal wind is eastward, they propagate upwards into the middle atmosphere with a velocity smaller than a critical value, which is a function of the horizontal wavenumber. This criterion is called the Charney-Drazin criterion (Charney and Drazin, 1961). PWs in the middle atmosphere have typical periods of 2 days to 16 days (Dunkerton, 1991; Salby, 1981a,b) and are assigned zonal wave numbers referring to the number of wave cycles along a given latitude circle.

PWs are most abundant in the Northern Hemisphere winter. The summer stratosphere has a mean westward zonal flow, and PWs cannot propagate during these conditions. The zonal distribution of water and land masses in the Northern Hemisphere are favourable for PW formation. PWs are also produced in the Southern Hemisphere, but they are much weaker, due to fewer mountain ridges and more open water (Shiotani and Hirota, 1985). Figure 2.4 shows the propagation of GWs and PWs during Northern Hemisphere winter and summer.

Amplitudes of both PWs and GWs increase as atmospheric density decreases with height. Eventually, waves break when their amplitudes grow large enough, depositing momentum and heat in the stratosphere and mesosphere (Eliassen and Palm, 1961). Vertically propagating GWs drive the residual circulation in the mesosphere by carrying eastward momentum and impos-

11

ing a drag that gives an equatorward meridional flow in summer. In winter, GWs carry westward momentum and impose a drag that gives a poleward meridional flow. PWs drive the circulation in the stratosphere by inducing a westward drag on the zonal flow and thus contributing to a meridional flow towards higher latitudes during wintertime: the Brewer-Dobson circulation (Holton, 2004). PWs are also driving forces behind sudden stratospheric warming events.

2.3. Sudden stratospheric warmings

The lack of heating in the polar stratospheric winter, due to little absorption of solar radiation by ozone, leads to the formation of the polar vortex, a core of cold air located above the winter pole, characterised by strong eastward zonal winds. In contrast, during summer, continuous heating of the polar stratosphere takes place, leading to a weaker temperature gradient between the equator and the pole and thus a weakening of the polar vortex (Schoeberl and Hartmann, 1991).

A sudden stratospheric warming (SSW) is the most dramatic event in the winter polar stratosphere. During an SSW, the polar vortex, stretching from the middle troposphere to the stratosphere, undergoes a strong temperature increase, in some cases as much as $50\,\mathrm{K}$ to $70\,\mathrm{K}$ in just a few days. The vortex is either disturbed and displaced from its typical location or split into two vortices, resulting in that the eastward zonal winds are slowed down or even completely reversed (Labitzke and Naujokat, 2000). According to the World Meteorological Organisation, an SSW is defined as *major* if at $10\,\mathrm{hPa}$ or lower altitudes the latitudinal mean temperature increases abruptly poleward from 60° latitude and the eastward zonal-mean winds reverse. If the temperature gradient is reversed, but not the circulation, the SSW is classified as *minor*. The Arctic polar vortex is less stable than the Antarctic because of the distribution of water and land masses, so SSWs are much more common in the Northern Hemisphere. In the Southern Hemisphere, only one major SSW event has ever been observed. This occurred in September 2002 (Dowdy et al., 2004).

PWs are driving forces behind SSW events, where they, by interacting with the mean zonal flow, have the power to weaken and disturb the polar vortex. The development of an SSW starts with the growth of planetary-scale disturbances (zonal wavenumbers 1 and 2) in the troposphere until they reach a large amplitude. PWs propagate into the stratosphere and give rise to a deceleration of the eastward jets and a weakening of the polar vortex. Zonal mean temperatures at high latitudes increase due to the waves. The westward acceleration of the zonal wind increases with increasing height, and at a certain level the winds reverse to westward. This level is called the critical

layer. PWs are absorbed at the critical layer and prevented from propagating further upwards. An intense warming of the polar cap region just below the critical layer is observed, due to Eliassen-Palm flux divergence of forced, upward-propagating PWs, and the westward winds are accelerated, lowering the level of warming and wind reversal (Matsuno, 1971).

SSWs not only impact the stratosphere. Mesospheric cooling and wind reversal are observed during SSW onset (e.g. Hoffmann et al., 2007; Labitzke, 1981). Observations show a downward propagation of circulation disturbances with an earlier onset of zonal wind reversal in the mesosphere compared with the upper stratosphere (Hoffmann et al., 2007). Proposed coupling mechanisms between the stratosphere and mesosphere during SSW events are related to PW and GW activity. Observations show evidence of increased wave number 1 PW and reduced GW activity in the mesosphere during SSW events. The mesospheric cooling is caused primarily by a relaxation of the polar mesosphere towards radiative equilibrium. This occurs as the westward winds induced by the SSW reduce transmission of GWs into the mesosphere (Holton, 1983).

2.4. Turbulence and the turbopause concept

Atmospheric turbulence is small-scale, irregular air motions due to winds that vary in speed and direction. Turbulence provides mixing of constituents, heat and energy in the atmosphere. The main sources are probably GWs and tides, which generate turbulence through non-linear breaking, shear instabilities, convective overturning and critical-level interaction (Hodges, 1967; Lindzen, 1981).

Two essential characteristics of turbulence are turbulent diffusion and turbulent energy dissipation. *Turbulent diffusion* is the transport or spreading of heat, momentum and tracer concentration due to irregular velocity fluctuations. *Turbulent energy dissipation* prevents an unlimited growth of turbulence. It is characterised by turbulent energy being cascaded successively to smaller and smaller eddies. At a very small scale, called the Kolmogorov microscale, the eddies are depleted, or dissipated, by viscous forces in the smallest eddies, and ultimately the energy is converted into heat (Kolmogorov, 1941; Reynolds, 1987). See Figure 2.5 for an illustration.

Atmospheric turbulence is important up to an upper altitude region ranging from 95 km to 110 km, varying on both a daily and a seasonal basis, where viscosity becomes so large that it damps any tendency for turbulence to form. This transition region is referred to as the turbopause (Hocking, 1987).

The turbopause may be defined in several ways, depending on measurement technique (Lehmacher et al., 2011). Blamont (1963) described a sudden transition from turbulent to laminar shapes becoming visible in sodium clouds
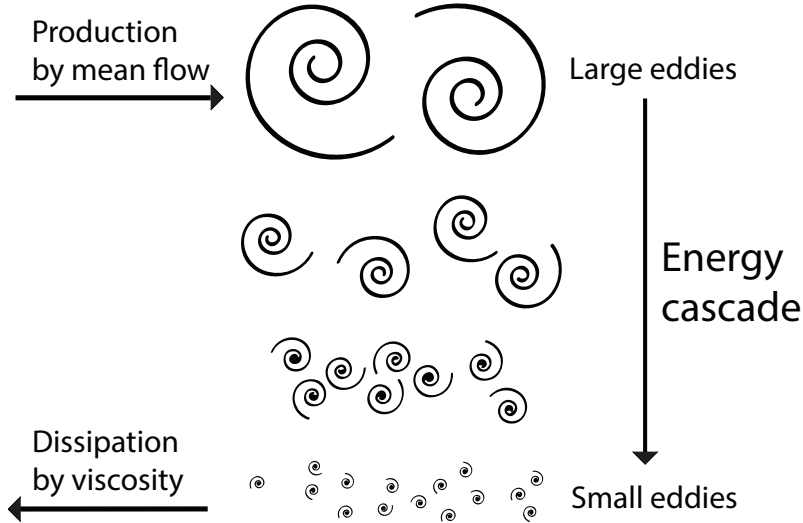
Figure 2.5.: Turbulent energy cascade.

ejected from rockets at an altitude varying between 95 km and 105 km. This can be referred to as the *visual turbopause*. Offermann et al. (2007) suggested the concept of a *wave turbopause*, which is based on the vertical distribution of wave dissipation and derived from standard deviations of vertical profiles of temperature variances. The turbopause may also be defined as the altitude where the eddy diffusion coefficient is equal to the molecular diffusion coefficient. It may be derived from mixing ratio profiles of particular species (Danilov et al., 1979) and is referred to as the *mixing turbopause*. In *Paper 3*, we have utilised the concept of the mixing turbopause and estimated the turbopause level by estimating turbulent energy dissipation rates using medium-frequency radar.

The turbopause may be defined in terms of the Reynolds number, *Re*, which is defined as the ratio of inertial forces to viscous forces in a fluid flow:

$$Re = \frac{\rho v L}{\mu} = \frac{v L}{\nu} \tag{2.1}$$

where ρ is the density of the fluid, v is mean velocity, L is characteristic length, μ is dynamic viscosity of the fluid and ν is kinematic viscosity (Reynolds, 1894).

The Reynolds number is dimensionless. If *Re* is large, we have turbulent flow. Contrary, if *Re* is small, we have laminar flow. Depending on the type of fluid, flow speed and the diameter of the flow, $Re < \sim 2300$ gives a laminar flow (Warhaft, 1997). At the turbopause, turbulent and molecular diffusivities are equal, and *Re* is unity.

2.5. Solar forcing

The atmosphere is not only affected internally through dynamics, but also by external forcing from above. The variability in the incoming solar shortwave radiation is known to drive changes in the atmosphere on decadal, annual and seasonal scales. The F10.7 cm solar radio flux, measured daily at the Penticton Radio Observatory in British Columbia, Canada, is one commonly used indicator of solar activity and correlates well with the sunspot number, as well as with a number of ultraviolet and visible solar irradiance records. During solar maximum, stronger dissociation of molecular oxygen by Lyman-α radiation takes place, leading to enhanced production of atomic oxygen. Lyman-α is a spectral line of hydrogen, emitted from the full solar disc with an integrated flux equivalent to the total solar emission at all wavelengths less than 150 nm, and thus it is a measure of solar activity (Lean and Skumanich, 1983). Airglow intensity is directly proportional to atomic oxygen concentration and hence correlated with the 11-year solar cycle (Grygalashvyly, 2015). Further details on the chemistry of the airglow layer will be given in Section 3.2.

It has been proposed that mesopause region airglow temperatures respond to solar activity also on shorter time scales. Solar flares and coronal mass ejections on the Sun may lead to energetic particles penetrating the atmosphere all the way down to the upper stratosphere. During solar proton events, high energy protons ionise molecules in the atmosphere, altering concentrations of odd hydrogen, nitrogen and oxygen, which again may deplete ozone in the mesosphere (e.g. Beig et al., 2008; Thomas et al., 1983). Since OH* airglow intensity and concentration in the mesopause are related to ozone concentration, which we will see in Section 3.2, mesopause region airglow may be influenced by short-term variations of solar activity. Scheer and Reisin (2007) investigated this for airglow temperatures mostly from El Leoncito (31.8°S), but they did not find signatures in their data that could convincingly be related to geomagnetic storms. The influence of solar activity on mesopause region temperatures on short time scales is not discussed in this PhD thesis.

2.6. Other influences on circulation and chemistry

The quasi-biennial oscillation (QBO) is a system where zonally symmetric eastward and westward wind regimes in the tropical stratosphere alternate regularly with a period varying from about 24 months to 30 months. Successive regimes propagate downwards from about 30 km at an average rate of 1 km month^{-1} (Lindzen and Holton, 1968). The QBO also influences the

circulation in the polar middle atmosphere (Holton and Tan, 1980). As an example is the frequency of SSWs affected by the phase of the QBO, where the westward phase is more associated with SSWs (Labitzke and Naujokat, 2000). The QBO is driven by vertically-propagating GWs, which are weakened by infrared cooling. Their momentum flux is deposited into the mean flow, leading to an oscillation in the mean flow (Holton and Lindzen, 1972).

Atmospheric tides are daily global-scale oscillations that can cause temperature amplitudes of more than $10\,\text{K}$ in the mesosphere. Tides are primarily forced by diurnal variations of the heating due to absorption of solar UV radiation by H_2O and O_3 (Andrews et al., 1987).

In this PhD work, mesopause temperature is mainly evaluated on time scales of months or years. Therefore, atmospheric tides on short time scales are not discussed.

3. Hydroxyl (OH*) airglow

Airglow is the emission of light by atoms and molecules excited through chemical processes and collisions in the middle and upper atmosphere. The emissions are produced when UV light from the Sun dissociates molecular oxygen into individual atoms during daytime (or periods of midnight sun). Atomic oxygen cannot efficiently recombine. Hence, its lifetime in the mesopause region is very long ($\sim$months), providing a "storage" of the chemical energy that powers the airglow during night time (or polar night). Different chemical reaction chains, involving atomic oxygen from the photodissociation of molecular oxygen, are responsible for the production of the excited states of atmospheric species. The excited atoms and molecules cascade to lower energy states by emitting light (photons), resulting in an emission spectrum over a wide wavelength range, from both the ultraviolet, visible and infrared part of the electromagnetic spectrum. The greatest contributions of airglow emissions are from the infrared. These are the brightest emissions in the night sky by far, but are beyond the visible spectrum range that we can see.

Excited atomic oxygen provides green (5577 Å) and red (6300 Å/6364 Å) emissions at 90 km to 100 km altitude and 150 km to 300 km altitude, respectively. Sodium atoms provide yellow light ($\sim$5890 Å) at a layer centred at $\sim$91 km. Excited molecular oxygen emits blue and near ultraviolet multi-wavelength banded radiation (3100 Å to 5000 Å) at $\sim$95 km height. Vibrationally and rotationally excited hydroxyl emits visible to infrared radiation at a layer centred at 87 km, where the near-infrared lines are the brightest (Chamberlain, 1961). Figure 3.1 shows layers of airglow enveloping Earth, observed from space.

Airglow can be divided into three groups depending on when it is observed, and the exact processes behind the three vary slightly. Airglow observed at night is called *nightglow*. During the day and at twilight it is referred to as *dayglow* and *twilightglow*, respectively. In this thesis, we have investigated nightglow data and are thus referring to nightglow when we use the term "airglow".

Airglow emissions are useful indicators of dynamical and chemical processes in the mesopause region. From airglow intensities, we can obtain temperatures of the mesopause region. This chapter elaborates on how this is possible, using emissions from the excited hydroxyl (OH*) molecule. Section 3.1.1 gives a short introduction to spectra of diatomic molecules, while Section 3.1.2 treats
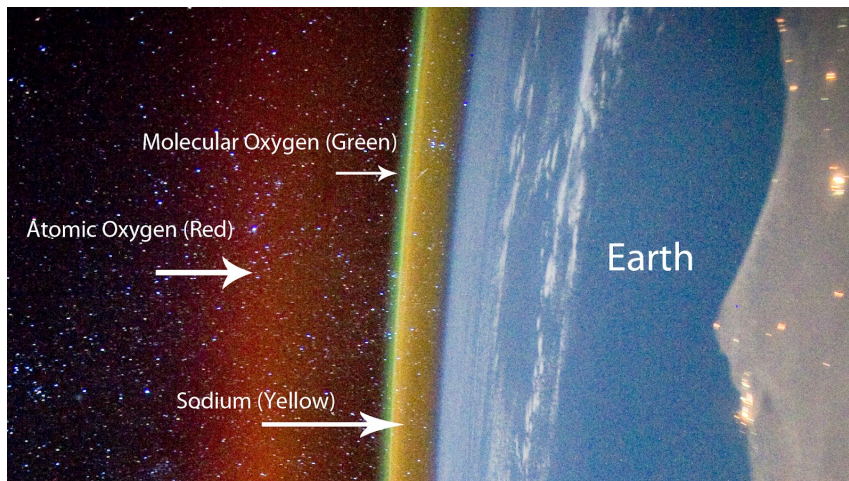
Figure 3.1.: Airglow layers created by light-emitting atoms and molecules in the middle and upper atmosphere. Image credit: NASA, with annotations by Alex Rivest.

OH* spectra in particular. Section 3.2 deals with the chemistry of OH* in the mesopause region. The method used for the retrieval of temperatures from the OH*(6-2) vibrational band is presented in Section 3.3. Finally, the instrumentation and data analysis are described in Section 3.4.

3.1. Molecular structure and spectra

3.1.1. Diatomic molecules

The theory behind the formation of emission spectra of diatomic molecules, which are molecules with two atoms, is described in detail in Herzberg (1950) and will briefly be repeated here. The total energy of a diatomic molecule is the sum of the electronic, vibrational and rotational energies:

$$E_{tot} = E_e + E_v + E_r \tag{3.1}$$

An atom or a molecule can only exist in energy states with certain discrete values.

A molecule can be in different *electronic states*, depending on the orbitals in which its electrons are. The state where all electrons have their lowest possible energies is referred to as the *ground state*. The electronic states of molecules are labelled and identified by their angular momentum and symmetry properties. The ground state is denoted *X*, while the excited states are denoted *A*, *B*, *C*, ...

A molecule's electrons have *orbital angular momentum*, **L**, associated with their orbit motion, and *spin angular momentum*, **S**, associated with the rota-

tion about their own axes. The total electronic angular momentum, $\boldsymbol{\Omega}$, is the vector sum of the two. In a diatomic molecule, the symmetry of the field in which the electrons move is reduced. There is only axial symmetry about the internuclear axis. The component of $\mathbf{L}$ along the internuclear axis is denoted Λ, and the constant component of the precession of $\mathbf{S}$ is denoted Σ. The total electronic angular momentum about the internuclear axis is defined as:

$$\Omega = \mid \Lambda + \Sigma \mid \tag{3.2}$$

Λ takes on discrete, positive values $0, 1, 2, ..., L$. The corresponding molecular state is represented by Greek letters Σ, Π, Δ, ... respectively, and is preceded by a symbol referring to the electronic state; *X*, *A*, *B*... See Eq. 3.8 for an example. Σ takes on values $S, S-1, S-2, ..., -S$, where S is non-negative integers or half integers, depending on whether the total number of electrons in the molecule is even or odd, respectively. Thus, Σ can, in contrast to Λ, be positive and negative and either integer or half integer.

Different values of $\Lambda + \Sigma$ correspond to different energies of the resulting molecular state. If $\Lambda \neq 0$ (that is, for Π, Δ, ... states), the electronic energy level splits into a so-called *multiplet* of $2S+1$ components. Molecules with an even number of electrons have odd multiplicities (singlets, triplets, ...), since S is integer. Conversely, molecules with an odd number of electrons have even multiplicities (doublets, quartets, ...), since S is half integer.

The electronic energy of the state, E_e, is given by the minimum value of the potential energy function of a given stable electronic state

$$E^{el} + V_n \tag{3.3}$$

where E^{el} is the electronic energy of the nuclei and V_n is the Coloumb potential, which is dependent on the nuclear charges and internuclear distance.

A diatomic molecule has two modes for motion. It can *rotate* about an axis passing through the centre of gravity, perpendicular to the line joining the nuclei. Also, the two atoms can *vibrate* relative to each other along the internuclear axis.

The simplest assumption of vibrational motion is that the diatomic molecule is a harmonic oscillator. This means that each atom moves towards or away from the other in simple harmonic motion. The displacement from equilibrium is a sine function of time. The vibrational energy of the harmonic oscillator is:

$$E_v = h\nu_{osc}\left(v + \frac{1}{2}\right) \qquad v = 0, 1, 2, ... \tag{3.4}$$

where h is Planck's constant and ν_{osc} is the vibrational frequency of the oscillator. v is the *vibrational quantum number*, which can take only values $\in \mathbb{N}_0$.

v describes vibrational energy levels, or energy states, of a molecule. Upper and lower vibrational quantum levels are denoted v' and v'', respectively. The energy for the harmonic oscillator is not zero in the state of lowest energy. Even in the lowest vibrational state, vibrational energy is present.

The simplest model of a rotating molecule is the so-called dumbbell model, where we consider two point masses, m_1 and m_2, fastened at a fixed distance r apart. The two masses rotate around the centre of gravity with a rotational frequency. The rotational energy of such a system is given by:

$$E_r = \frac{h^2 J(J+1)}{8\pi^2 I} \qquad J = 0, 1, 2, ... \tag{3.5}$$

where I is the moment of inertia of the system and J is the *rotational quantum number*, which can take only values $\in \mathbb{N}_0$. J represents rotational angular momentum, and in the absence of external electric or magnetic fields, the energy level depends only on the molecule's change in angular momentum. Thus, we have a series of discrete energy levels whose energy increases quadratically with increasing J.

A diatomic molecule can undergo transitions from one rotational energy level to another through absorption or emission of a photon. This results in spectral lines which can be detected by a spectrometer. J' and J'' denote the upper and lower rotational quantum levels, respectively, and ΔJ is the difference between them. Not all rotational transitions are allowed. Quantum mechanical selection rules determine that:

$$\Delta J = J' - J'' = \begin{cases} -1 \\ 0 \\ 1 \end{cases} \tag{3.6}$$

Different variations of ΔJ correspond to different *branches of lines*. $\Delta J = -1$ corresponds to the so-called P branch of the lines, $\Delta J = 0$ corresponds to the Q branch, and $\Delta J = 1$ corresponds to the R branch.

The above descriptions of simple models for rotating and vibrating diatomic molecules are idealised and represent observed spectra to a good approximation. However, sometimes large deviations from these idealised models are observed, due to that rotation, vibration and electronic motion take place simultaneously, and that these motions influence each other. This matter will not be further elaborated on here.

The emission wavelength, λ, of a diatomic molecule is determined by the energy difference of a transition between an upper and a lower molecular state:
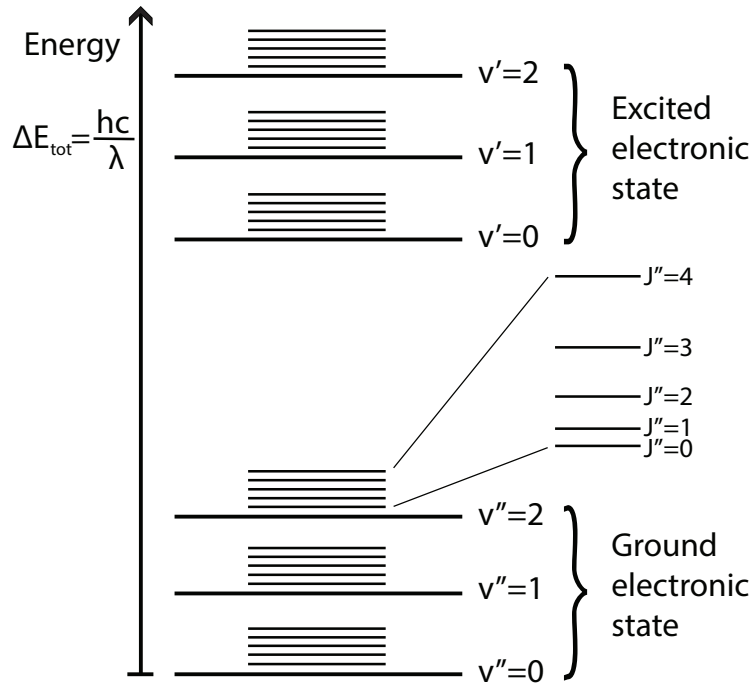
Figure 3.2.: Schematic of energy levels of a diatomic molecule. The electronic energy levels are widely separated compared to the vibrational levels. The rotational levels are even more closely situated than the vibratonal levels. For legibility, only the lowest levels are presented. Figure is not drawn to scale.

$$\lambda = hc/(E_{v'} - E_{v''} + E_{J'} - E_{J''})$$
$$= (G(v') - G(v'') + F(v', J') - F(v'', J''))^{-1} \tag{3.7}$$

where c is the speed of light and E is energy of the states. $G(v)$ is the vibrational term in vibrational state v and $F(v,J)$ is the rotational term in vibrational state v and rotational state J. ' and " denote upper and lower states, respectively.

Electronic energy is by far the largest contributor to the total energy. The vibrational energy states give a fine structure to the electronic states, while the rotational energy states give a fine structure to the vibrational states, see Figure 3.2.

The upper and lower states can differ in electronic, vibrational and rotational states. Molecules undergoing transitions from a higher vibrational and rotational state to a lower state results in the formation of *molecular spectra* composed of *vibrational bands*, which again consist of *rotational lines.* Figure 3.4 shows the nightsky spectrum between 1200 Å and 9000 Å.

3.1.2. **OH***

In this PhD thesis, we denote the hydroxyl emissions OH^* to emphasise that we refer to the vibrationally and rotationally excited hydroxyl airglow. OH* airglow emission bands were first described in detail by Meinel (1950a,b). OH* in the mesopause is in its electronic ground state designated by

$$X^2\Pi_{\frac{3}{2}} \quad and \quad X^2\Pi_{\frac{1}{2}} \tag{3.8}$$

The splitting into two states is due to that OH* is in a doublet state, and this is annotated by the left superscript to Π (the number 2). The annotation Π corresponds to that Λ equals 1. The right subscripts to Π, $\frac{3}{2}$ and $\frac{1}{2}$, correspond to total electronic angular momentum, Ω, and from Eq. 3.2 it follows that Σ can be either $-\frac{1}{2}$ or $+\frac{1}{2}$. This is due to that the electron spin can be either up or down, which is an effect of the odd number of electrons, as described in the previous section.

The $X^2\Pi_{\frac{3}{2}}$ state gives rise to the so-called P_1, Q_1 and R_1 branches, while the $X^2\Pi_{\frac{1}{2}}$ state gives rise to P_2, Q_2 and R_2. The $X^2\Pi_{\frac{1}{2}}$ state lies higher than the $X^2\Pi_{\frac{3}{2}}$ state, which makes the P_2, Q_2 and R_2 line intensities weaker than P_1, Q_1 and R_1 in the lower, more populated state. Consequently, there is an alternation in intensity between P_1 and P_2 lines.
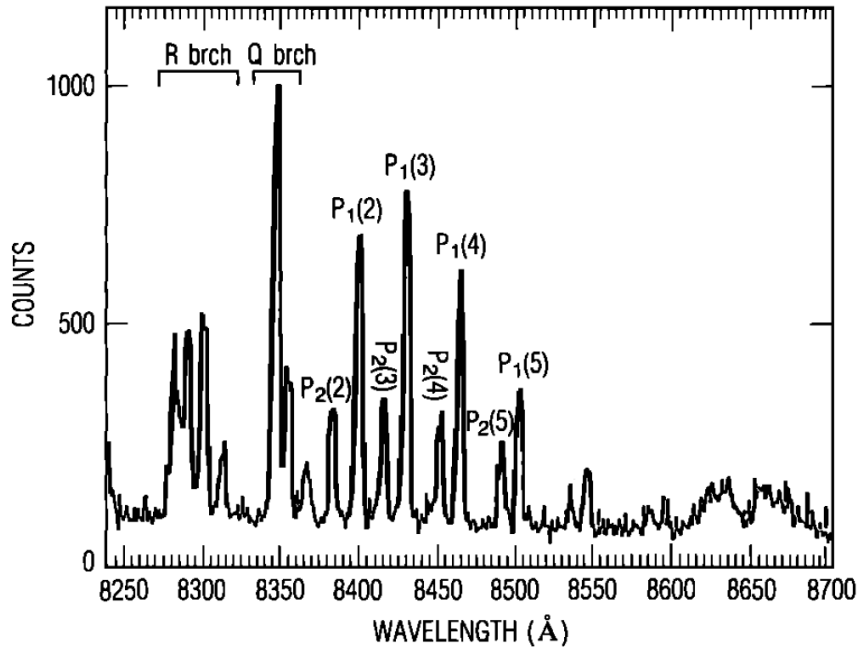
Figure 3.3.: Spectrum of the OH*(6-2) vibrational band, averaged over a half-hour period, recorded with a $\frac{1}{2}$ m Ebert-Fastie spectrometer in Longyearbyen. From Sivjee and Hamwey (1987).

In this PhD project, we have used spectra from the OH*(6-2) vibrational band to calculate rotational temperatures, meaning the OH* band with the transition from $v' = 6$ to $v'' = 2$. The emission wavelengths of OH*(6-2) are $\sim$8400 Å. Figure 3.3 shows the P, Q and R branches of OH*(6-2).

According to Eq. 3.7 in the previous section, the emission wavelength of a diatomic molecule can be determined if the energies of the upper and lower molecular states are known. The energy levels can be deduced if the vibrational and rotational terms are known. The vibrational term for OH*(6-2) is:

$$G(v) = \omega_e \left(v + \frac{1}{2}\right) - \omega_e x_e \left(v + \frac{1}{2}\right)^2 + \omega_e y_e \left(v + \frac{1}{2}\right)^3 - \omega_e z_e \left(v + \frac{1}{2}\right)^4 + ... \quad (3.9)$$

where ω_e, $\omega_e x_e$, ... are vibrational constants taken from Chamberlain and Roesler (1955) and listed in Table 3.1.

The two rotational terms of OH*(6-2), corresponding to the two states $X^2\Pi_{\frac{3}{2}}$ and $X^2\Pi_{\frac{1}{2}}$, are determined by the formulae of Hill and Van Vleck (1928):

$$F_1(v, J) = B_v \left[\left(J + \frac{1}{2}\right)^2 - 1 + \frac{1}{2}\sqrt{4\left(J + \frac{1}{2}\right)^2 + Y_v\left(Y_v - 4\right)}\right] - D_v J^4 \quad (3.10)$$

$$F_2(v, J) = B_v \left[\left(J + \frac{1}{2}\right)^2 - 1 - \frac{1}{2}\sqrt{4\left(J + \frac{1}{2}\right)^2 + Y_v\left(Y_v - 4\right)}\right] - D_v J^4 \quad (3.11)$$

where B_v, D_v and Y_v are rotational constants calculated by Krassovsky et al. (1962) and listed in Table 3.1. Figure 3.5 shows vibrational structure, as well as rotational structure of vibrational levels of the OH* $X^2\Pi$ ground state.

3.2. Chemistry of the OH* layer

3.2.1. Production and loss of OH* in the polar mesopause region

Excited hydroxyl in the polar mesopause region is produced mainly by these reactions:
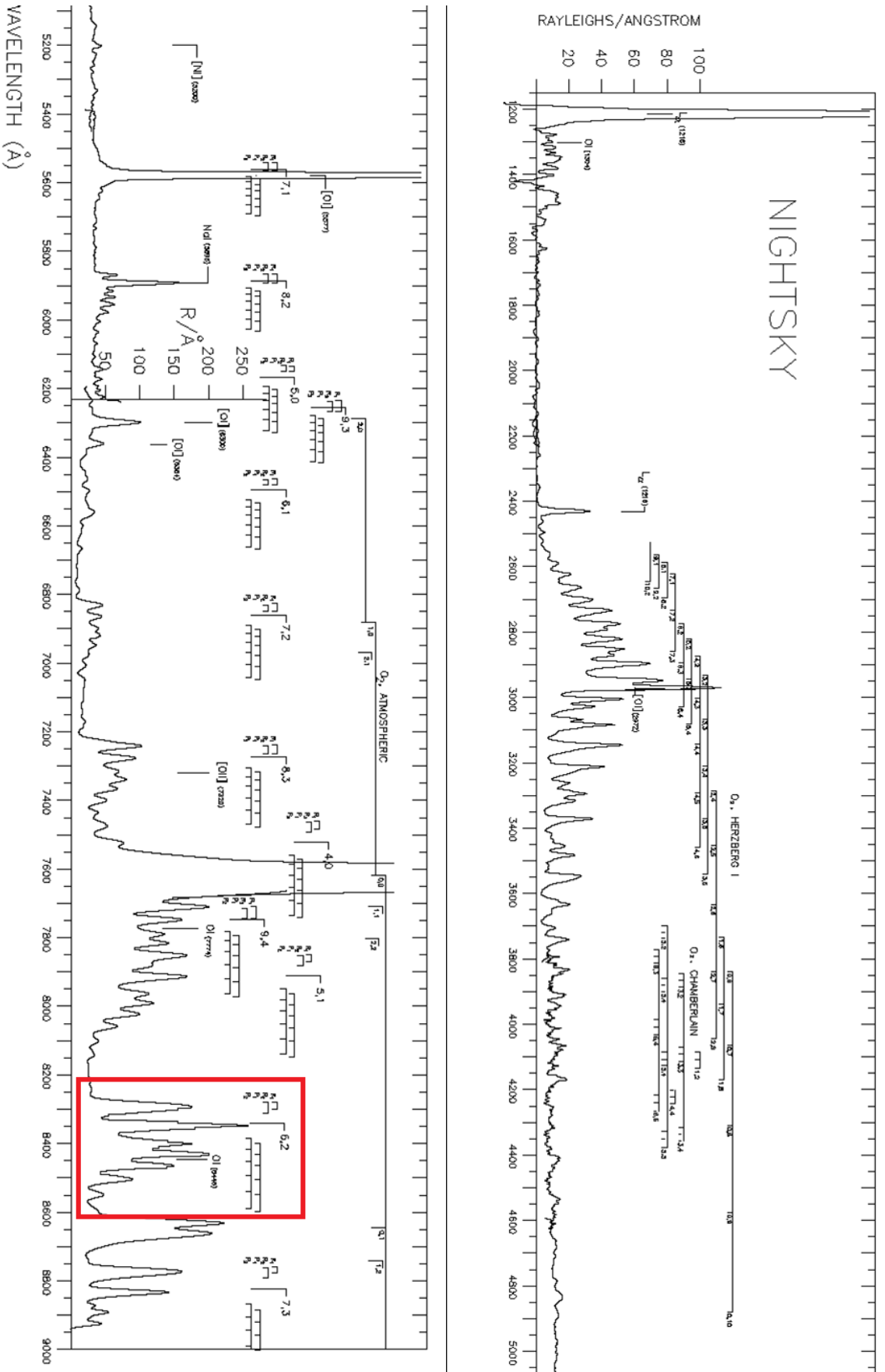
Figure 3.4.: Nightsky spectrum between 1200 Å and 9000 Å, recorded in December 1992 by Ultraviolet Spectroscopy and Imaging Group, University of Arizona. The OH*(6-2) vibrational band is highlighted.
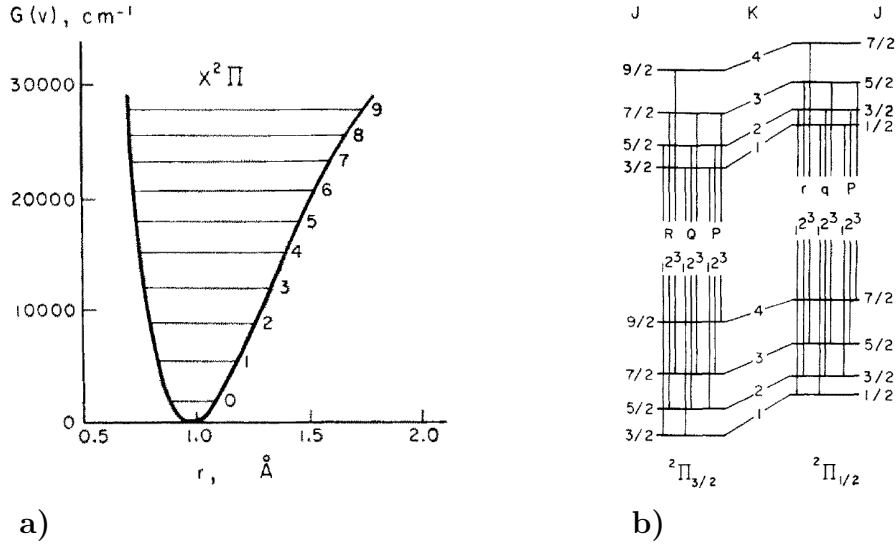
Figure 3.5.: a) Potential curve of the OH* $X^2\Pi$ ground state, showing vibrational structure. b) Rotational structure of vibrational levels. From Krassovsky et al. (1962).

$$O_3 + H \longrightarrow OH^*(v' \leq 9) + O_2 + 3.3 eV \qquad (3.12)$$
$$HO_2 + O \longrightarrow OH^*(v' \leq 6) + O_2 + 2.3 eV \qquad (3.13)$$
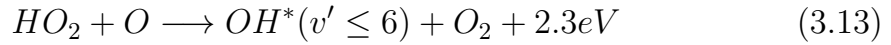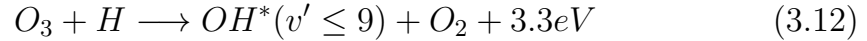
The ozone-hydrogen mechanism (Eq. 3.12) is considered the dominant source of OH* on a global basis (Bates and Nicolet, 1950), but the perhydroxyl-oxygen mechanism (Eq. 3.13) is the source of up to half of the OH*(v' $\leq$ 6) observed in the winter mesopause over Svalbard, due to the absence of photodissociation of HO_2 (Sivjee and Hamwey, 1987). The lower vibrational levels of OH*(v') are, in addition to the reactions above, believed to be pop-

Table 3.1.: Vibrational and rotational constants for OH*(6-2), taken from Chamberlain and Roesler (1955) and Krassovsky et al. (1962). Units are cm^{-1} for all constants except Y_v, which is dimensionless.

Vibrational constants		Rotational constants	v=6	v=2
ω_e	3737.90	B_v	14.349	17.108
$\omega_e x_e$	84.965	D_v	0.0018	0.0018
$\omega_e y_e$	0.5398	Y_v	-9.795	-8.214
$\omega_e z_e$	0.01674			
$\omega_e q_e$	-0.001637			

ulated as a result of either radiative cascade from the higher levels (Eq. 3.14) or stepwise collisional deactivation processes by atomic oxygen and molecular nitrogen and oxygen (Eq. 3.15) (Grygalashvyly, 2015; McDade, 1991):

$$OH^*(v) \longrightarrow OH^*(v') + h\nu \tag{3.14}$$
$$OH^*(v) + M \longrightarrow OH^*(v-1) + M \tag{3.15}$$
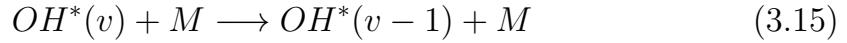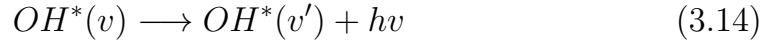
where v and v' denote the upper and lower vibrational levels, respectively. M is a non-reactive body, in this case O, O_2 and N_2. $h\nu$ denotes the energy of the photon emitted.

Loss mechanisms for OH*(v') in the mesopause are quenching by atomic oxygen, molecular nitrogen and molecular oxygen (Eq. 3.16), chemical removal by atomic oxygen (Eq. 3.17) and radiative cascade to lower levels (Eq. 3.18) (Grygalashvyly, 2015):

$$OH^*(v') + M \longrightarrow OH^*(v'-1) + M \tag{3.16}$$
$$OH^*(v') + O \longrightarrow H + O_2 \tag{3.17}$$
$$OH^*(v') \longrightarrow OH^*(v'') + h\nu \tag{3.18}$$
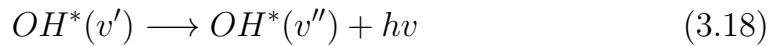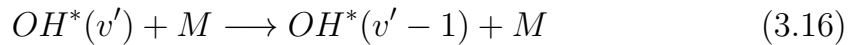
where M is O, O_2 and N_2. v' and v'' denote the upper and lower vibrational levels, respectively. Quenching by molecular oxygen is considered the main loss mechanism (Adler-Golden, 1997).

3.2.2. Distribution and variation of OH*

Height distribution

The OH* emissions are centred at around 87 km altitude with a mean thickness of 8 km, according to rocket measurements (Baker and Stair, 1988). The balance between the rapid fall-off in ozone concentration with height and the more frequently occurring collisional quenching by atmospheric constituents at lower atmospheric levels is the reason why the OH* airglow layer is centred near 87 km height.

Different vibrational states of OH* have different emission peak altitudes. Bands originating from higher vibrational levels have higher emission peak altitudes than bands originating from lower levels. This is, according to the study by von Savigny et al. (2012), associated mainly with quenching by atomic oxygen. von Savigny et al. used a collisional cascade model to determine the effect of atomic and molecular oxygen on the dependence of observed vibrational levels. They found that the greatest contribution came from quenching by atomic oxygen. They explained this by the strong increase

of atomic oxygen concentration with increasing altitude. Hence, at higher altitudes, the lower vibrational levels are more strongly quenched by atomic oxygen relative to at lower altitudes, leading to decreasing populations of the lower vibrational states here.

Diurnal variation of OH*

The concentration of OH* in the mesopause varies according to the concentration of other atmospheric species. When the sun is up, it dissociates O_3 and O_2 according to these reactions:

$$O_3 \longrightarrow O_2 + O \qquad O_2 \longrightarrow 2O \qquad (3.19)$$
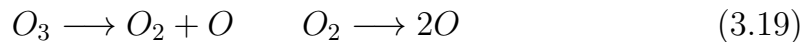
Thus, during daytime (or periods of midnight sun) we have high concentrations of O compared to O_2 and O_3, and hence, from Eq. 3.12, low concentrations of OH*. When the sun sets, rapid recombination of O back into O_2 and O_3 starts, according to, amongst others, these reactions:

$$2O \longrightarrow O_2 \qquad O + O_2 + M \longrightarrow O_3 + M \qquad (3.20)$$
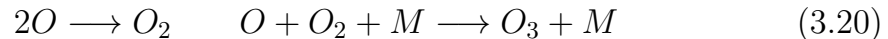
where M is a non-reactive body (Chapman, 1931). Since O is abundant during daytime, O_3 rapidly starts forming when the sun sets. Hence, the OH* concentration and intensity increase rapidly from about 5 degrees solar depression angle, which corresponds to sunset at 90 km height. At some point, the O_3 production slows as O concentration decreases. As a result, the OH* concentration and intensity decrease. Hence, OH* intensity and temperature tend to experience a small increase just after sunset, followed by a decrease (Patrick Espy, pers. comm., 2016). The diurnal variation of OH* has not been investigated in this PhD thesis.

Annual variation of OH*

The number density and peak height of the OH* layer at nighttime at high latitudes are directly proportional to atomic oxygen concentration (Grygalashvyly, 2015). The highest number densities and lowest altitudes of the OH* layer are found in winter. This corresponds to downwelling of air associated with the annual variation of the mesospheric residual circulation and thus downward mixing of atomic oxygen from the ionosphere into the polar mesopause region. Conversely, upwelling of air during summer decreases atomic oxygen concentration and hence OH* density (Liu et al., 2008).

3.2.3. Effects of energetic particle precipitation on OH* airglow

As mentioned in Section 2.5, there is an ongoing investigation whether energetic particle precipitation (EPP) may affect OH* intensity and temperature. EPP creates odd nitrogen ($NO_x = NO$, NO_2) in the middle atmosphere, which affects ozone chemistry (Newnham et al., 2013, and references therein). Hence, EPP may affect the OH*. EPP produces odd nitrogen in the 80 km to 90 km region, which reacts with atmospheric species according to these reactions (Brasseur and Nicolet, 1973):

$$NO + O_3 \longrightarrow NO_2 + O_2 \qquad (3.21)$$

$$NO_2 + O \longrightarrow NO + O_2 \qquad (3.22)$$

$$Net \quad O_3 + O \longrightarrow 2O_2$$
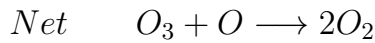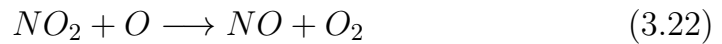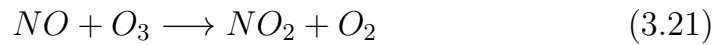
Hence, in theory, one way EPP may affect the OH* is by reducing the amount of O_3 available in the mesopause region. Reaction 3.21 must compete with reaction 3.12 in order to remove O_3 and in this way reduce the OH* production. However, reaction 3.21 is slower than reaction 3.12. This could, in theory, be compensated by a higher NO production, but there is never enough NO present in the airglow region for reaction 3.21 to equal reaction 3.12, not even during heavy geomagnetic storms.

A way EPP can affect OH* concentration is through altering concentrations of O, following reaction 3.22. The equilibrium of the reactions above shifts according to the amount of O present in the 80 km to 90 km height region. The more O available, the greater tendency of equilibrium towards NO, since reaction 3.22 then occurs frequently. The less O available, the greater tendency of equilibrium towards NO_2, since reaction 3.22 occurs not so frequently. To conclude, we have less O available to form O_3 and hence OH* in the mesopause with NO present, produced by EPP (Patrick Espy, pers. comm., 2016).

3.3. Retrieval of OH*(6-2) temperatures

OH* rotational temperature can be derived from the intensities of rotational lines, and the intensity of each rotational line can be expressed as:

$$I_{v',J' \rightarrow v'',J''} = N_{v',J'} A_{v'J' \rightarrow v'',J''} \qquad (3.23)$$

where $N_{v',J'}$ is the total concentration of OH* molecules in the highest rotational level and $A_{v'J' \rightarrow v'',J''}$ is the transition probability, or the total rate at

which radiative transitions occur between *v'* and *v"* (Mies, 1974). *A* is also called Einstein coefficient. In *Paper 1* and *Paper 2*, we have used Einstein coefficients from Mies (1974).

When deriving temperatures from the rotational distribution of OH*, we assume that the OH* molecules in the mesopause are following a Boltzmann distribution. A Boltzmann distribution gives the probability that a system will be in a certain state as a function of that state's energy and the temperature of the system, and assumes thermodynamical equilibrium (Gibbs, 1902). Reaction 3.12 produces OH* in highly excited rotational states, such that the initial rotational distribution is non-Boltzmann for energy states with very short radiative lifetimes. OH* (v' > 2) undergo on the average at least 10 collisions before emitting photons and thus have relatively long radiative lifetime, which indicates local thermodynamical equilibrium (Sivjee, 1992). Further discussion on this matter can be found in *Paper 2*. The assumption of a Boltzmann distribution of the rotational levels in a certain vibrational state allows us to express the total concentration of molecules in the highest rotational level as:

$$N_{v',J'} = N_{v'} \frac{2(2J'+1)}{Q_r} e^{\frac{-F(J')hc}{kT_{rot}}} \tag{3.24}$$

where Q_r, the electronic-rotational partition function for the *v'* levels, is defined as:

$$Q_r = \sum_{J'} 2(2J'+1) e^{\frac{-F(J')hc}{kT_{rot}}} \tag{3.25}$$

$F(J')$ is the upper rotational term, $N_{v'}$ is the total number of molecules in the system, k is the Boltzmann constant and T_{rot} is rotational temperature (Mies, 1974). Q_r can also be expressed as:

$$Q_r = 1 + 3e^{\frac{-2B_v hc}{kT_{rot}}} + 5e^{\frac{-6B_v hc}{kT_{rot}}} + ... \approx \frac{kT_{rot}}{B_v hc} \tag{3.26}$$

The approximation in Eq. 3.26 holds for sufficiently large T or small B_v and is valid for OH* in the mesopause (Herzberg, 1950). Combining Eqs. 3.23, 3.24 and 3.26 yields:

$$I_{v',J' \to v'',J''} = N_{v'} A_{v',J' \to v'',J''} \frac{2(2J'+1)hcB_v}{kT_{rot}} e^{\frac{-F(J')hc}{kT_{rot}}} \tag{3.27}$$

In Eq. 3.27, both $N_{v'}$ and T_{rot} are unknowns. Therefore, it is only possible to calculate the relative line strengths, making it necessary to have at least two lines in a rotational-vibrational band to obtain a temperature. Taking the logarithm of Eq. 3.27 gives:

Figure 3.6.: The Kjell Henriksen Observatory.

$$ln\left(\frac{I_{v',J'\to v'',J''}}{2(2J'+1)A_{v',J'\to v'',J''}}\right) = ln\left(\frac{N_{v'}hcB_v}{kT_{rot}}\right) - \frac{F(J')hc}{kT_{rot}} \tag{3.28}$$

Plotting $ln(\frac{I}{2(2J'+1)A})$ against the rotational term F(J') should yield a straight line when the system is in thermodynamical equilibrium and is referred to as a Boltzmann plot. Rotational temperatures can be derived from the slope of a linear fit to the Boltzmann plot.

3.4. Experimental

The Ebert-Fastie spectrometer, that has been providing OH* airglow spectra in this study, is located in Longyearbyen, Svalbard. From 1983 to 2007, the measurements were conducted at the Auroral Station in Adventdalen (78.20°N, 15.82°E), about 4 km away from town. In 2007, the spectrometer was moved to the Kjell Henriksen Observatory (KHO) (78.15°N, 16.04°E), see Figure 3.6. An increasing demand for more space at the Auroral Station led to the construction of a new and modern observatory. KHO is located at 520 m altitude, at the mountain Breinosa, approximately 15 km from the centre of Longyearbyen. Figure A.2 in the Appendix shows the locations of the old station relative to the KHO. For most of the year, the road to the KHO is partly covered with snow and is only accessible with track-laying vehicle, which makes the location remote and favourable with respect to artificial light pollution from town, cars and snowmobiles.

In Longyearbyen, the Sun remains below the horizon for nearly four months during winter. This allows for uninterrupted diurnal measurements of OH* airglow around winter solstice.

3.4.1. 1 m Ebert-Fastie spectrometer

The 1 m focal length Ebert-Fastie spectrometer scans the wavelength region between 8240 Å and 8705 Å in first order, enveloping the P branch of the OH*(6-2) vibrational band. Instrumental bandpass is 5 Å. The instrument scans one spectrum every 25 s. Field of view is approximately 5 degrees in the zenith direction. The cone angle is slightly larger in the direction parallel to the entrance slit, which results in an area of measurement of $\sim$9 km $\times$ 12 km at 90 km altitude. A photo of the spectrometer together with experimental setup are shown in Figure 3.7. Further details on the spectrometer can be found in Sigernes et al. (2003).
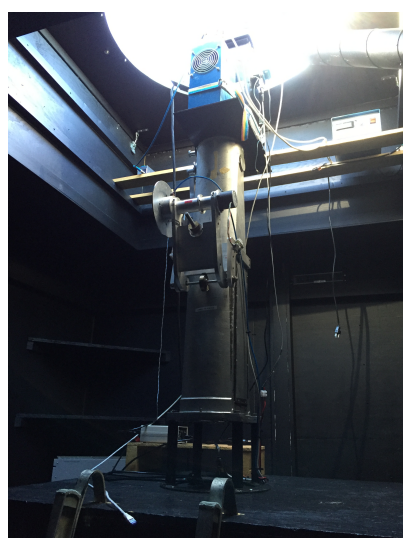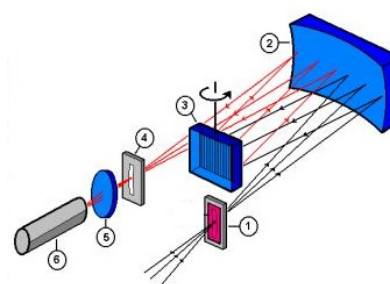
1 Entrance slit
2 Mirror
3 Rotating grating
4 Exit slit
5 Exit optics
6 Detector

a)   b)

Figure 3.7.: Photo (a) and experimental setup (b) of the Ebert-Fastie spectrometer located at the KHO, Longyearbyen. Experimental setup sketch courtesy of Fred Sigernes, UNIS.

Measurements of OH* airglow intensities in Longyearbyen using Ebert-Fastie spectrometers date back to the late 1970s. From 1983, intensity measurements of the OH*(6-2) band have been conducted on a regular basis. Measurements are conducted from November through February, when the Sun is 10° or more below the horizon.

A number of papers on OH* airglow rotational temperatures obtained from Ebert-Fastie spectromenters in Longyearbyen have been published in the last three decades. The focus of research during the 1980s was mainly on seasonal and diurnal variations, gravity wave interactions and sudden stratospheric warming events (Myrabø, 1984; Myrabø et al., 1984; Sivjee et al., 1987; Viereck and Deehr, 1989; Walterscheid et al., 1986). The last decade, the focus has been mostly on trends, coupling mechanisms and methods for

inferring OH* peak layer heights (Dyrland et al., 2010; Dyrland and Sigernes, 2007; Mulligan et al., 2009; Sigernes et al., 2003).

3.4.2. Data analysis

As described in Section 3.3, there are two unknowns in the equation we have for solving the rotational temperature, T_{rot}, and it is therefore only possible to calculate the relative strengths of the rotational lines. In this PhD project, we have derived rotational temperatures from measured spectra with the aid of synthetic spectra. The technique used is described as follows.

First, we made hourly averages of the measured airglow spectra. After calculating a linear background, synthetic spectra were iterated to fit the measured spectra. The background was found by linearly fitting an offset value to data points at the background level in between the specific emission lines. Furthermore, all hourly spectra were passed through a procedure for classifying them as "good" or "poor". The selection criteria for "good" spectra were based on experience and consistency for the whole dataset and are listed in *Paper 2*. Spectra were classified as "poor" e.g. when the background level was high, due to scattering of moonlight or artificial light from clouds, or when we had contamination by the auroral line OI 8446 Å, which is located close to the $P_2(4)$ line. We derived temperatures from the slope of a linear fit to a Boltzmann plot using $P_1(2)$, $P_1(3)$, $P_1(4)$ and $P_1(5)$ rotational line intensities of the OH*(6-2) vibrational band. These particular P_1 lines were chosen since rotational lines originating from states higher than J'=5 may not be in local thermodynamical equilibrium (Pendleton et al., 1993). The corresponding P_2 lines ($P_2(3)$, $P_2(4)$ and $P_2(5)$) were ensured to follow the same fit, even though they were not used for the temperature retrieval. If the P_2 fit is not close to the P_1 fit, the local thermal equilibrium assumption fails. We performed the sorting of data and calculation of rotational temperatures using the IDL program Spekkis and the Delphi program SyntheticOH (Sigernes et al., 2003). Figure 3.8 shows an hourly averaged spectrum of OH*(6-2) with a corresponding Boltzmann plot, handled in SyntheticOH. Further explanations on the temperature retrieval method can be found in *Paper 1* and *Paper 2*.

3.4.3. Uncertainties and limitations of OH* rotational temperature measurements

It is important to have in mind that a change in derived OH* temperature may be due to either a temperature change within the height distribution of OH*(6-2), a change in the height distribution itself, or a combination of both. We have discussed this matter in *Paper 2*, but the discussion will be repeated here. Ground-based instruments like the Ebert-Fastie spectrometer

measure the column-integrated emission rate contributed from the whole layer and lack height information. The fundamental study by Baker and Stair (1988) revealed that the mean altitude for the OH* emission layer peak height is around 87 km and that the mean emission layer thickness is about 8 km. However, several studies have addressed that the peak height of OH* emissions appears to vary with both season, local time, dynamical conditions and solar forcing (Dyrland et al., 2010; Liu and Shepherd, 2006; Shepherd et al., 2005; Yee et al., 1997). Also, OH* emissions originating from different vibrational bands peak at slightly different altitudes (von Savigny et al., 2012).

One option is to model the peak emission altitude, using OH* band intensities (integrated emission rates) measured by spectrometer and altitude profiles of OH* emission rates retrieved from satellite, as proposed by Mulligan et al. (2009). Mulligan et al. investigated peak emission altitude of the OH* layer over Svalbard using data from SABER (Sounding of the Atmosphere using Broadband Emission Radiometry) on board the TIMED (Thermosphere Ionosphere Mesosphere Energetics and Dynamics) satellite for parts of the 2003/2004 winter season. They found an inverse relationship between OH* peak altitude and emission rate, and provided a method for inferring peak altitude of the OH* emission layer using OH* integrated emission rates measured by spectrometer.

Thus, in theory, it is possible to acquire information about the altitude of the OH* layer and OH* temperatures simultaneously. However, TIMED was launched in December 2001, almost two decades after the beginning of the Longyearbyen OH* airglow temperature record. Also, SABER is in its southward-looking mode from mid-November to mid-January. In this period, which coincides with a large part of the OH* airglow measuring season, it is not covering the latitude at which Longyearbyen is located. We have not used Mulligan et al.'s method for modelling the peak emission altitude of the OH* layer in this PhD project.

Studies have shown that absolute values of derived OH* airglow temperatures may vary, depending on the choice of rotational transition probabilities and on the vibrational level of the transition's upper state (Cosby and Slanger, 2007; Noll et al., 2015; Turnbull and Lowe, 1989). However, studying OH* airglow temperatures on a long time scale, for instance by assessing long-term trends, and by looking at only one vibrational band, as is done in *Paper 2*, these matters are of less concern and have not been further elaborated in this PhD thesis.

Another limitation of the OH* airglow measurements is that the measurements are only conducted during night time/polar night. Also, spectra can be contaminated by aurora and scattering of moonlight or artificial light by clouds.
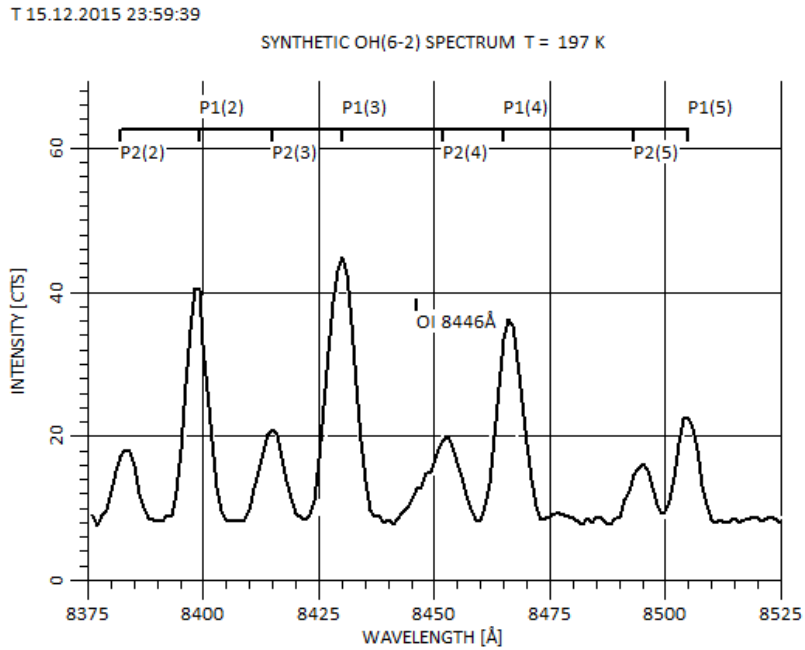
a) Spectrum of OH*(6-2), obtained by the 1 m Ebert-Fastie spectrometer on 15 December 2015 over Longyearbyen. Rotational lines from the P branch are denoted, as well as the OI 8446 Å auroral line, which contaminates the spectrum.
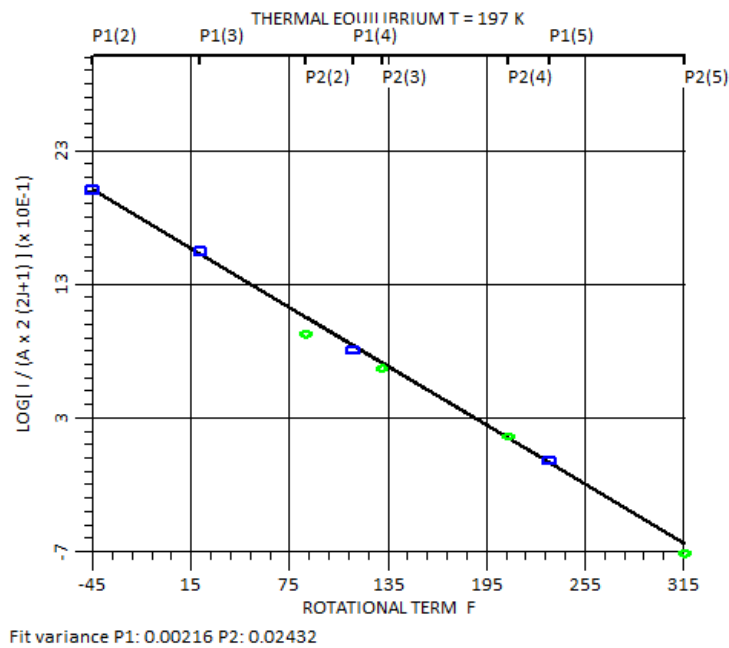
b) Boltzmann plot corresponding to the spectrum in a). Blue squares denote P_1 line intensities, while green triangles denote P_2.

Figure 3.8.

4. Atmospheric measurements using radar

While Chapter 3 described how we can retrieve temperatures from hydroxyl airglow, this chapter treats methods for retrieving atmospheric parameters using radar. In Section 4.1, the theory behind deriving temperature using meteor radar is presented, as well as a description of the instrumentation. The theory behind the derivation of turbopause height from turbulent energy dissipation rates using medium-frequency radar is presented in Section 4.2.

4.1. Mesopause temperatures derived from meteor echo fading times

4.1.1. From meteoroid to meteor echoes

A *meteoroid* is a small solid object ($10\,\mu m$ to $1\,m$) which travels in outer space (Rubin and Grossman, 2010). Some meteoroids enter Earth's atmosphere, where they are slowed down by friction with atmospheric gas molecules. The object is now called a *meteor*. The kinetic energy is converted into heat, and, entering the MLT region, this heat is sufficient to sublime and ionise the atoms and molecules at the surface of the meteor. The loss of mass from the surface of the meteor by sublimation is called *ablation*. The surrounding atmospheric gas is ionised as well. Most meteors are destroyed in the MLT region, due to ablation and to fragmentation because of the increasing aerodynamic pressure.

Meteor ablation results in a plasma trail that expands radially. This is due to *ambipolar diffusion*, which will be explained in the following section. Radio waves, sent from radars located at the ground, are scattered by the plasma trail. The scattering is divided into two categories, depending on whether the number of electrons produced per meter of path length is smaller or greater than a certain critical value. This corresponds to the plasma frequency being smaller or larger than the radar frequency. If smaller, the meteor trail is *underdense*, which means that the radio wave penetrates the plasma column freely, and each electron acts as an individual scattering source. If greater, the meteor trail is *overdense*, which means that the radio wave is reflected from the surface layer of the trail. It is the underdense echoes that are used

when deriving temperatures from meteor radars. If the trail is underdense, the echo received by the radar decays exponentially with a time constant, determined by the ambipolar diffusion coefficient and the wavelength of the radio wave (McKinley, 1961).

4.1.2. Ambipolar diffusion

Derivation of temperatures from meteor radar is based on the principle of ambipolar diffusion. The effect of ambipolar diffusion occurs in as ionised gas consisting of electrons and ions, as they move out in an electrically neutral cloud (McKinley, 1961). A meteor trail is an example of such an ionised gas. In a meteor plasma trail, electrons and ions move outwards with their respective thermal velocities. Due to their high temperature and low mass, the electrons' thermal velocities are higher than those of the ions. As the electrons move, they will leave behind the slower ions and a positive charge density, and an electric field will appear. The electric field will act on the charged species, slowing the more mobile electrons and accelerating the less mobile ions. When the diffusion flux of the positive charges equals that of the negative charges, the electrical current is zero, and we have ambipolar diffusion. The ambipolar diffusion coefficient is a measure of how fast the diffusion process is.

4.1.3. Retrieval of neutral temperatures from meteor radar

Assuming that ambipolar diffusion is the sole agent responsible for the decrease of electron density in a meteor trail, the backscattered radio wave amplitude from an underdense trail decreases exponentially with time, t, as

$$A(t) = A_0 e^{\frac{-t}{\tau}} \tag{4.1}$$

where A_0 is the wave amplitude at $t = 0$, typically at the time when exponential decay begins. τ is the measured echo decay time, which is the time it takes for the amplitude to fall to e^{-1} of its maximum value, expressed as:

$$\tau = \frac{\lambda^2}{16\pi^2 D_a} \tag{4.2}$$

where λ is the radar wavelength and D_a is the ambipolar diffusion coefficient (Jones, 1975). The assumption that ambipolar diffusion alone determines the rate of decay of echoes is valid for the altitude range $85\,\text{km}$ to $95\,\text{km}$, as shown by e.g. Jones (1975), Hall et al. (2005), Ballinger et al. (2008) and discussed in *Paper 4*.

The Einstein diffusion relation states that for a collection of ions in a neutral gas, diffusion is related to ambient temperature and mobility of the ions:

4.1. Mesopause temperatures derived from meteor echo fading times

$$D_i = \frac{k_B T_i K}{e} \tag{4.3}$$

where D_i is the ionic diffusion coefficient, k_B is Boltzmann constant, T_i is ion temperature and e is elementary charge. K is the zero-field mobility factor of the ions, which is the ions' ability to move through the gas in response to an electric field. We may write the ion mobility in terms of a "reduced mobility", K_0, by correcting K to standard gas density. K_0 at standard temperature and pressure is defined by the equation (Cervera and Reid, 2000; McDaniel and Mason, 1973):

$$K = \frac{1.013 \times 10^5}{p} \frac{T}{273.16} K_0 \tag{4.4}$$

Usually, a value for K_0 between $1.9 \times 10^{-4}\, \mathrm{m^2\, s^{-1}\, V^{-1}}$ and $2.9 \times 10^{-4}\, \mathrm{m^2\, s^{-1}\, V^{-1}}$ is chosen, depending on what ion one assumes to be the main ion of the trail (Hocking et al., 1997).

The ambipolar diffusion coefficient is, in the case of a negligible magnetic field, expressed as:

$$D_a \simeq D_i \left(1 + \frac{T_e}{T_i}\right) = 2D_i \tag{4.5}$$

where T_e is electron temperature (Kaiser, 1953). Eq. 4.5 is valid for electrons and ions in thermal equilibrium in a meteor trail. Combining Eqs. 4.3, 4.4 and 4.5 gives the following relation between D_a, T and P:

$$D_a = 6.39 \times 10^{-2} \frac{T^2}{p} K_0 \tag{4.6}$$

Solving for T gives:

$$T = \sqrt{\frac{D_a p}{6.39 \times 10^{-2} K_0}} \tag{4.7}$$

The temperature estimate thus depends on D_a, which we obtain from the meteor decay time, τ (Eq. 4.2), pressure p and mobility factor K_0. Measurements of atmospheric pressure are difficult to obtain at 90 km height. In this PhD work, pressure values have been derived from atmospheric densities obtained from falling sphere measurements appropriate for 70°N, combining those of Lübken and von Zahn (1991) and Lübken (1999). In *Paper 4*, a value of $2.4 \times 10^{-4}\, \mathrm{m^2\, s^{-1}\, V^{-1}}$ was chosen for K_0, following Cervera and Reid (2000) and Holdsworth et al. (2006). Variations of K_0 have been further elaborated in *Paper 4*.

4.1.4. Nippon/Norway Tromsø Meteor Radar

The Nippon/Norway Tromsø Meteor Radar (NTMR) is located at Ramfjordmoen research station (69.58°N, 19.22°E), approximately 13 km from Tromsø, Norway. Figure A.3 in the Appendix shows the location of Ramfjordmoen relative to Tromsø. Most ground-based observations of the upper atmosphere from mainland Norway are conducted here. The NTMR was installed in November 2003 and is jointly operated by Tromsø Geophysical Observatory, which is a part of The University of Tromsø - The Arctic University of Norway, and National Institute for Polar Research, Japan. The meteor radar is operating at 30.25 MHz, and transmitting power is 7.5 kW (peak). It consists of one transmitter and five receiver antennas. All antennas are 3-element crossed Yagis. Field of view is approximately 70° off zenith. Figure 4.1 shows an image of one of the antennas, as well as the configuration of the antennas.

The NTMR detects decay times of echoes from ionised meteor trails in the MLT region. The decay times can be used to derive ambipolar diffusion coefficients, D_a, using Eq. 4.2, which again can be used to arrive at neutral temperatures in the height region ∼85 km to ∼95 km, using Eq. 4.7. Echoes are detected from a region within a radius of approximately 100 km (horizontal space), and around 10000 echoes are typically detected per day. The height and range resolution are both 1 km when looking at altitudes around the peak occurrence height of 90 km.

Publications of data retrieved from the NTMR during the last decade have treated temperatures and diffusivities (e.g. Hall et al., 2006, 2005b), winds (e.g. Hall et al., 2005a), as well as dynamics and dynamic changes in the MLT region (Hall and Tsutsumi, 2013; Kurihara et al., 2010).

4.1.5. Limitations and advantages of using a meteor radar for acquiring mesopause temperatures

A great advantage of the NTMR is that it is operated 24 hours a day, all year round, and that it conducts measurements regardless of cloud cover. The radar detects 200–600 echoes per hour at the peak occurrence height (90 km). The total number of detected meteor echoes results in sufficiently good statistics to allow for a 30 min temporal resolution. Another advantage is that the operational frequency of the radar is such that a simple time of flight estimation can be utilised to obtain the altitude of the meteor trails. From this we get the distance between the meteor echo and the radar, and hence we obtain the altitude of the meteor trails. This is contrary to e.g. airglow measurements, which yield temperature from the entire vertical column of the emitting airglow layer.

Using the NTMR for obtaining mesopause temperatures is advantageous,

a) One of the six identical antennas which constitute the Nippon/Norway Tromsø Meteor Radar. Image credit: Chris Hall.
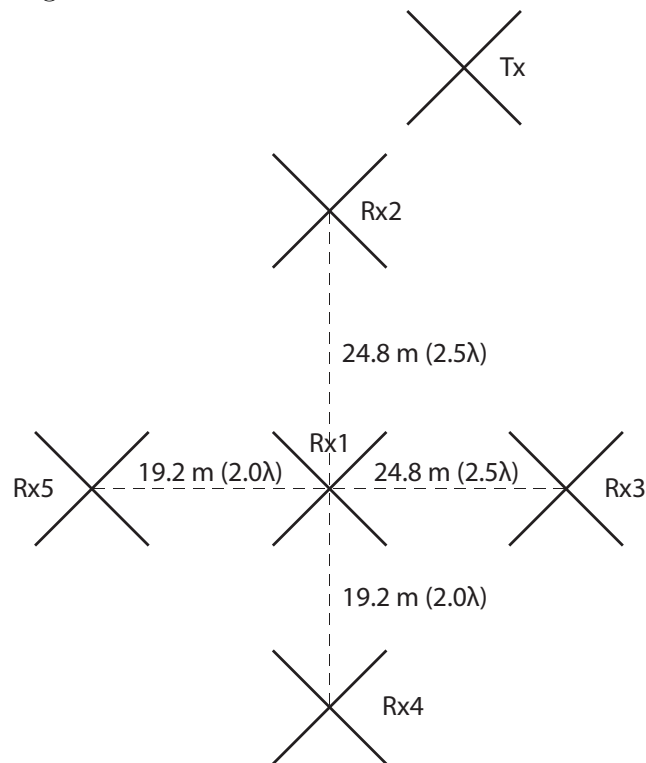
b) Sketch of the antenna configuration. Tx denotes the transmitting antenna, Rx1–5 denote the receiving antennas.

Figure 4.1.

due to that the detected meteor echoes are more evenly distributed, both spatially and temporally, compared to echoes detected at a low-latitude station. Meteor and planetary orbits are roughly coplanar, which means that they are on the same geometric plane. This results in that at high latitudes, many meteors traverse the field of view, contrary to at low latitudes, where there is a tendency of dawn head-on arrival of meteors.

We have thoroughly discussed the limitations of the meteor radar in *Paper 4*. In summary, the drawbacks for retrieving neutral temperatures are mostly associated with uncertainties in values chosen for pressure and the mobility factor. Using ambipolar diffusion coefficients derived from meteor radar measurements to calculate neutral atmospheric temperatures requires pressure values from the corresponding altitude. Measurements of pressure are rare at 90 km height, and often one has to rely on pressure values from models.

There is a possibility that D_a derived from the NTMR can be affected by modified electron mobility during auroral particle precipitation. In *Paper 4*, unrealistic enhancements of D_a due to particle precipitation were briefly investigated. Investigations concluded that approximately 5 % of hourly D_a values were unrealistic and hence rejected from further analysis.

The meteor radar is suitable for estimating neutral temperatures at around 90 km altitude. Above ~95 km, gradient-drift Farley-Buneman instability may cause measured fading times higher than expected from ambipolar diffusion alone, leading to an underestimation of derived ambipolar diffusion coefficients (Ballinger et al., 2008; Dyrud et al., 2001; Kovalev et al., 2008). Below ~85 km, higher diffusivity than expected according to theory may be encountered, due to reasons not fully understood (Hall et al., 2005b). Younger et al. (2014) attribute the higher diffusivity in the lower parts of the meteor region to chemically-induced neutralisation of underdense meteor plasma, initiated by three-body attachment of positive meteoric ions to neutral atmospheric molecules.

4.2. Turbopause height derived from turbulent energy dissipation rates

4.2.1. Turbulent energy dissipation rates

Measurements of turbopause altitude are difficult to conduct, mainly because direct measurements of small-scale fluctuations in neutral density, temperature and motion at around 100 km height are virtually impossible (Hall et al., 2008). One way of locating the turbopause is by estimating turbulent energy dissipation rates, ϵ, which are rates at which turbulent kinetic energy is converted into thermal internal energy, as explained in Section 2.4. ϵ is derived

4.2. Turbopause height derived from turbulent energy dissipation rates

from the conservation equation for turbulent kinetic energy.

From the fading times, or decay times, of backscattered signals received by a medium-frequency (MF) radar, we can obtain a measure of the intensity of turbulence (Hocking, 1983). The turbulent kinetic energy of the air may be represented by v'^2, which is the variance of wind velocity fluctuations, v', relative to the background wind, v. The relation between v' and radar echo fading times can be expressed as:

$$v' = \frac{\lambda\sqrt{ln2}}{4\pi\tau_c} \tag{4.8}$$

where λ is the radar wavelength and τ_c is the characteristic fading time of the signal (Briggs, 1980). The rate of dissipation of the turbulent kinetic energy is obtained by dividing by a characteristic time scale, since

velocity variance $\approx$ kinetic energy per unit mass
energy dissipation rate $\approx$ (kinetic energy per unit mass) per unit time

The Brunt-Väisälä period, $T_B = 2\pi/\omega_B$, where ω_B is the Brunt-Väisälä frequency, is proposed as a characteristic time scale. Since non-turbulent dynamics also can affect the signal fading times (will be further elaborated in Section 4.2.3), the estimates of turbulent energy dissipation rates obtained from radar measurements must be regarded as maximum values, or upper limits for turbulent energy dissipation present in the atmosphere (Hall, 2001). We therefore designate the estimates of turbulent energy dissipation rates obtained from radar ϵ_{max}. ϵ_{max} may be expressed as:

$$\epsilon_{max} = \frac{0.8v'^2\omega_B}{2\pi} \tag{4.9}$$

The factor 0.8 comes from an average of gravity waves over all directions in three dimensions (Weinstock, 1978).

The minimum energy dissipation rate, ϵ_{min}, present in the atmosphere, due to viscosity, is given by:

$$\epsilon_{min} = \frac{\omega_B^2\nu}{\beta} \tag{4.10}$$

where ν is kinematic viscosity and $\beta \equiv R_f/(1 - R_f)$ is the mixing or flux coefficient, related to the flux Richardson number, R_f. β lies between 0.2 and 1 (Hocking, 1987) and varies according to the assumed dominant turbulence scale. A large β is proposed for very large eddies. In *Paper 3*, a value of 0.3 has been chosen for β. This is in accordance with e.g. Fukao et al. (1994), who assume that the dominant turbulence scale is slightly smaller than the buoyancy scale.
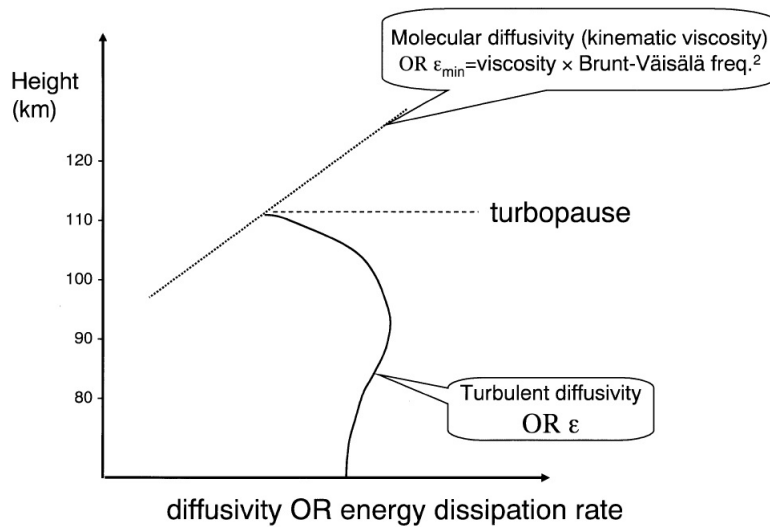
Figure 4.2.: Schematic presentation of the definition of the turbopause used in this PhD work. From: Hall (2001).

ϵ_{max} includes energy dissipation from all processes. In order to isolate those not related to viscosity, we end up with this expression for the turbulent energy dissipation rate, ϵ:

$$\epsilon = \epsilon_{max} - \epsilon_{min} \tag{4.11}$$

The height of the turbopause is identified as the altitude where $\epsilon = \epsilon_{min}$, which is where the energy dissipation rate corresponds to only molecular diffusion. See Figure 4.2 for an illustration.

4.2.2. Medium-frequency (MF) radar

The MF radar system at Ramfjordmoen became operational in 1975, as the first instrument of the research station. The radar is a collaboration between The University of Tromsø - The Arctic University of Norway, Nagoya University (Japan) and University of Saskatchewan (Canada). The purpose of the radar is to monitor winds and turbulence between 60 km and 120 km height. The radar is operating at 2.78 MHz, and transmitter power is 50 kW (peak). Transmission is performed through a 4 × 4 crossed dipole array, while reception is performed on three inverted V antennas arranged in an equilateral triangle. Height and time resolutions are 3 km and 5 min, respectively. Figure 4.3 shows an image of parts of the antenna system and the configuration of the antennas. Further details on the radar can be found in Hall (2001) and in *Paper 3*.

The principle behind the radar is that it illuminates irregularities in electron

a) Parts of the MF antenna system located at Ramfjordmoen research station, Tromsø. Image credit: Tromsø Geophysical Observatory.
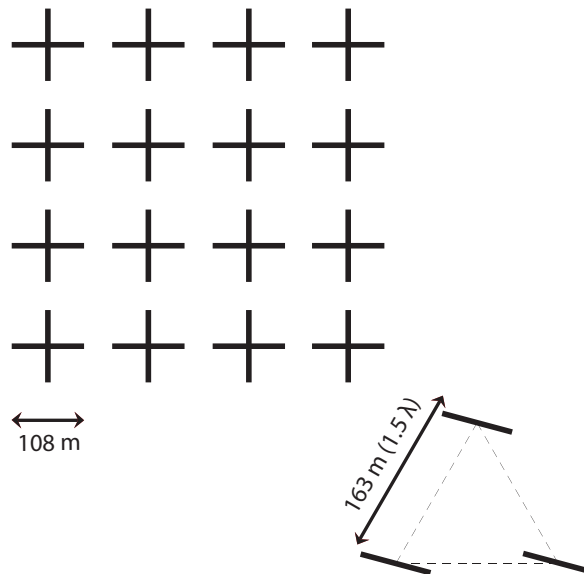
b) Configuration of the antennas. Transmission is performed through a 4 × 4 crossed dipole array, while reception is performed on three inverted V antennas.

Figure 4.3.

density, and backscatter from these structures forms a moving diffraction pattern at the ground, which is recorded by spaced antennas. The radar beam propagates vertically, surviving repeated partial reflections until being totally reflected by the high electron densities in the E region of the ionosphere. The reflected structures are moved by the background wind and perturbed by shorter timescale dynamics. Cross-correlations between signals received at the different antennas yield horizontal wind vector, typically between 50 km and 100 km height. Autocorrelations yield characteristic fading times of the echoes, which can be interpreted as turbulent intensity (Hall et al., 2008).

From the echo fading times, we may derive wind velocity fluctuations of the air, v' (Eq. 4.8). Furthermore, we get estimates of ϵ_{max} and therefore ϵ from v'^2 (Eqs. 4.9 and 4.11). Neutral atmosphere temperature (in the calculation of the Brunt-Väisälä frequency) and density (in the calculation of kinematic viscosity) are obtained from the NRLMSISE-00 Atmosphere Model (Picone et al., 2002).

Results from measurements obtained from the Tromsø MF radar have been widely published over a period of four decades. During the 1970s and early 1980s, research was mostly focused on investigations of electron density (e.g. Brekke et al., 1985; Hargreaves and Brekke, 1981), while investigations of winds were initialised in the early 1990s (e.g. Manson and Meek, 1991; Manson et al., 1992; Singer et al., 1994). Dynamical features like tides, GWs and PWs were investigated during the 1990s and 2000s (e.g. Forbes et al., 1994; Luo et al., 2002; Manson et al., 1999, 1990a,b). Eddy velocities estimated from characteristic fading times were estimated as early as 1978 (Schlegel et al., 1978), but it was not until the late 1990s that the estimation of turbulent intensities was continued and turbopause height was investigated (e.g. Hall et al., 2007, 1998a,b, 2008).

4.2.3. Instrument limitations and advantages

The Tromsø MF radar offers a height resolution of 3 km, meaning that it cannot be used to obtain detailed information about turbulent structure. The advantage of the radar is that it is able to examine gross features of turbulence in an altitude region which is inaccessible to other, higher-resolution techniques. Field of view is 15° off zenith, which means that the MF radar covers a smaller volume compared to e.g. the meteor radar, which estimates wind over a larger area. A smaller field of view indicates less interference of horizontal motions, e.g. GWs, which can shorten fading times (Hocking, 1983, 1985).

A drawback of using an MF radar to estimate turbulent energy dissipation rates is that the derived rates seem to be estimates of the upper limit for where turbulent kinetic energy is dissipated, due to an overestimation of fading

rates (Hocking, 1983). A radio wave is refracted slightly when it encounters small changes in the atmospheric conditions, e.g. changes in temperature, pressure, humidity or electron density irregularities. The radio wave will be more delayed the higher up into the ionosphere it goes, as electron density increases through the D region and lower E region, especially during heavy particle precipitation events. Thus, on occasion, we assume that the echo comes from a higher altitude than it actually does. As a consequence of this, the turbopause height estimated from turbulent energy dissipation rates from MF radar may be underestimated.

5. Main results

This chapter contains the main findings from *Papers 1–4*. Results from research conducted in this PhD work can be divided into two main categories: *seasonal variability* of mesopause region temperatures and *trends* of temperatures and turbopause height. In the following sections, we discuss and compare the results from the two locations – Tromsø and Longyearbyen – with results from other locations. Finally, we reflect briefly on the limitations of the work done in this PhD thesis.

5.1. Seasonal variability of polar mesopause region temperatures

5.1.1. OH*(6-2) airglow temperatures from Longyearbyen

We examined winter season variations of temperatures derived from OH*(6-2) airglow above Longyearbyen by performing a superposed epoch analysis of the temperatures (*Paper 1*). A superposed epoch analysis involves sorting all daily temperatures by day of year and then computing the means of all days of the year. In this way, a climatology is obtained. A 5-day running mean was applied in order to arrive at a winter climatology for the Longyearbyen OH*(6-2) dataset (Figure 4, *Paper 1*). We identified local temperature maxima in mid-January and mid-February, as well as a minimum in the transition between December and January.

5.1.2. Meteor radar temperatures from 90 km height over Tromsø

We applied Lomb-Scargle periodogram analysis to the daily temperatures from 90 km height obtained from the NTMR to identify periodic oscillations in the dataset (*Paper 4*). A Lomb-Scargle periodogram analysis is a method used for estimating a frequency spectrum based on a least-squares fit of sinusoids to a dataset and is a powerful way to find periodic signals. It is a modified discrete Fourier transform algorithm, and, contrary to discrete Fourier transform, suitable for unevenly spaced data (Lomb, 1976; Scargle, 1982). We found a number of statistically significant (>95 %) oscillations

with time scales ranging from 9 days to a year. The annual, semi-annual, ter-annual and quatra-annual oscillations were particularly pronounced.

We superposed daily temperatures by day of year and applied a least-squares fit, using periodic components found in the Lomb-Scargle analysis (see Figure 7, *Paper 4*). The seasonal variation showed higher temperatures and variability during winter compared to summer. We also found local temperature enhancements, or reduction of the strong seasonal negative gradient, just after spring equinox and summer solstice.

Temperature variability and seasonal variation may, to a large extent, be explained by the large-scale circulation in the middle atmosphere and corresponding wave activity. Higher temperature variability in winter is due to the presence of upward-propagating PWs during this season, in contrast to summer, when westward winds are blocking vertical propagation of long-period PWs into the MLT region. The particularly high variability in January and February is probably related to the occurrence of SSW events, which are more abundant at that time of year. Temperature increase after spring equinox, as seen in the seasonal variation, is related to the final breakdown of the polar vortex, as suggested by Shepherd et al. (2002). The local temperature increase during summer is most likely due to a combined effect of upward-propagating GWs and interhemispheric propagation of PWs, as found by e.g. Stray et al. (2014) and Hoffmann et al. (2010). The seasonal variation also showed a local temperature minimum around day 340, which we at this point lack physical explanations for.

5.1.3. Similarities/differences between Longyearbyen and Tromsø and comparison with other locations

The two datasets are not directly comparable, since the temperature retrieval methods are different. Also, the Longyearbyen time series contains only temperatures from November through February, while the Tromsø record is from all year round. As a consequence of this, we will not perform a thorough comparison between the two datasets. Nevertheless, a brief comparison of temperature variation during winter reveals some differences between the two datasets. While the Longyearbyen dataset shows a temperature minimum in the transition between December and January, the Tromsø dataset shows a local minimum around day number 340, corresponding to the beginning of December. Also, the pattern of higher variability in January and February in Tromsø temperatures is not apparent in the Longyearbyen dataset. The Longyearbyen dataset displays high variability throughout the winter.

The periodic components found in the NTMR temperature dataset have also been identified in datasets from other mid-latitude and high-latitude sites, e.g. Espy and Stegman (2002) (OH*(3-1) temperatures from Stock-

holm, 59.5°N), French and Burns (2004) (OH*(6-2) temperatures from Davis, Antarctica, 68.6°S) and Bittner et al. (2000) (OH*(3-1) temperatures from Wuppertal, 51°N). Bittner et al. (2000) and French and Burns (2004) also found additional sub-annual periodic oscillations, as well as other shorter-period components, in their datasets.

The local temperature minumum around day 340, found in the NTMR dataset, is found neither in the Stockholm nor the Davis temperatures. The Stockholm temperatures experience a minimum during the first days of the year (Figure 3, Espy and Stegman (2002)), more similar to the Longyearbyen OH*(6-2) dataset. Temperatures from Davis show a local decrease in July–August, corresponding to Northern Hemisphere January–February, which is completely different behaviour compared to our results.

It is difficult to conclude on what the reasons for different seasonal variability between the datasets are. The datasets may experience different seasonal variation due to that the locations may be influenced by different orographic and meteorological conditions, which again may influence the forcing from waves propagating from below.

5.2. Polar mesopause trends

5.2.1. OH*(6-2) airglow temperatures from Longyearbyen

We updated the OH* airglow temperature record from Longyearbyen with data from the winter seasons 2005/2006 to 2012/2013 (*Paper 1, Paper 2*) using the approach described in Section 3.4.

We subtracted the winter climatology, described in *Paper 1* and summarised in Section 5.1.1, from daily OH* temperatures to obtain residual temperatures. A multivariate regression fit was applied to the residuals to detect a long-term trend coupled with solar response. Solar response was investigated by looking into three different measures of solar variation: the F10.7 cm solar radio flux, the sunspot number and total solar irradiance. The highest correlation was achieved between OH* temperatures and total solar irradiance, but only slightly higher than for the other two. Due to that the F10.7 cm solar radio flux is the most commonly used measure of solar variability and the result therefore is easier to compare with other studies, the solar response coefficient was estimated using F10.7. We estimated the solar response coefficient, from the regression, to be $(3.6 \pm 4.0)\,\mathrm{K}/100\,\mathrm{SFU}$, and the trend from 1983 to 2013 was estimated to $(-0.2 \pm 0.5)\,\mathrm{K\,decade^{-1}}$ (*Paper 2*). The magnitude of the solar response coefficient is on the same level as results obtained from other mid-latitude and high-latitude sites (French and Klekociuk, 2011; Offermann et al., 2010; She and Krueger, 2004).

Also, we investigated monthly trends (*Paper 2*). All winter months showed

a positive trend, except for December. However, uncertainties are high, implying that the results from the monthly trend analysis are difficult to interpret.

5.2.2. Meteor radar temperatures from 90 km height over Tromsø

Before estimating a trend, we calibrated NTMR daily temperatures with respect to temperatures measured by the Microwave Limb Sounder on board the EOS (Earth Observing System) Aura spacecraft (*Paper 4*). This was necessary due to that ambipolar diffusion coefficients derived from meteor radar depend on both ambient atmospheric temperature and pressure. Due to lack of pressure measurements, we used pressure estimates obtained from falling spheres during the 1990s, appropriate for 70°N (Lübken, 1999; Lübken and von Zahn, 1991) in the temperature calculation.

We estimated the NTMR temperature trend from the approximation to the least-squares, composite fit of the sinusoids corresponding to periodic oscillations identified in the dataset. Temperature response to solar variability was not analysed, due to that the length of the time series was shorter than the corresponding solar cycle. We estimated an overall trend of $(-2.2 \pm 1.0)\,\mathrm{K\,decade^{-1}}$ from 2003 to 2014, while summer and winter trends were estimated to $(-0.3 \pm 3.1)\,\mathrm{K\,decade^{-1}}$ and $(-11.6 \pm 4.1)\,\mathrm{K\,decade^{-1}}$, respectively (*Paper 4*). Only the winter trend was considered significantly non-zero and detectable, following criteria in Weatherhead et al. (1998) and Tiao et al. (1990).

The most accepted theory behind a cooling of the middle atmosphere involves increased greenhouse gas emissions, but this matter still remains unsolved. The lack of response in the mesopause region compared to e.g. the stratosphere is, according to Schmidt et al. (2006), explained by changes in dynamics. Some dynamical processes contribute to a warming which counteracts the cooling expected from greenhouse gas emissions.

A less cooling trend in summer compared to winter may be explained by an increase in CO_2 radiative forcing, leading to a larger heat exchange from underlying layers, as the summer mesopause is considerably colder than the relatively warm layers below. Thus, we get a stronger equator-to-pole temperature gradient and stronger mid-latitude tropospheric westerlies. The result is a weakening of the GW drag on the MLT region and decreased adiabatic cooling (Fomichev et al., 2007; Schmidt et al., 2006). The net effect is a stronger cooling of the middle atmosphere in winter compared to summer, consistent with our results.

5.2.3. Similarities/differences between Longyearbyen and Tromsø and comparison with other locations

Due to that airglow intensities over Longyearbyen are only measured during winter, we can only compare winter trends from the two locations. The winter temperature trend for Tromsø is considerably more negative than the Longyearbyen trend. Other studies on long-term mesopause temperature trends from mid-latitude and high-latitude sites report mostly negative or near-zero trends (e.g. French and Klekociuk, 2011; Offermann et al., 2010). This is in line with the Longyearbyen OH*(6-2) winter trend, and the summer and overall trend of the Tromsø temperatures.

Beig (2011) states that there has been a shift in long-term trend assessments during the last decade from near-zero trends to negative trends. The author emphasises that a trend analysis is a snapshot of the time period covered, and that one of the reasons why different trend results vary is that the measurement periods differ. Hence, the different time spans may be one reason why the Tromsø winter temperature trend is significantly more negative than the Longyearbyen trend.

Other reasons for the deviating results can be that we compare temperatures obtained using different methods. The NTMR temperatures are obtained from 90 km geometric altitude, while the spectrometer, providing the OH*(6-2) temperatures, measures the column-integrated emission rate contributed from the whole airglow layer. Also, we used slightly different definitions of "winter" in the two trend assessments.

5.2.4. Turbopause height over Tromsø and comparison with other locations

We derived turbopause altitude estimates from turbulent energy dissipation rates obtained from the MF radar in Tromsø and investigated trend in altitudes. The height of the turbopause is located roughly around 100 km during summer and around 105 km in winter. We found an increasing height during the time period from 2001 until 2015 in summer, $(1.6 \pm 0.3)\,\mathrm{km\,decade^{-1}}$, while in winter turbopause height did not change significantly (*Paper 3*). We investigated the response of the change in turbopause heights to changing temperature (*Paper 4*), but changing temperature did not alter trends significantly, irrespective of season.

Paper 3 also treats turbopause height over Saskatoon, Canada (52°N, 107°W). Results show that turbopause height over Saskatoon does not change significantly over the time period from 1999 to 2014, regardless of season. We will not discuss the results from Saskatoon further in this PhD thesis. Other turbopause height trend studies that cover the same time period are few.

Oliver et al. (2014) analyse incoherent scatter radar measurements of ionospheric temperature and density above Millstone Hill (42.6°N, 71.5°W) over the years 1976 to 2013. They find a long-term atomic oxygen density increase at 120 km height and suggest that a descent in turbopause height can explain the increase. By visual examination (Oliver et al., 2014, Figure 6, bottom panel), a *decrease* in atomic oxygen density is evident from 2001 onwards. Following the suggestion of Oliver at al., this corresponds with an increase of turbopause height, which is in accordance with our results.

The exact mechanisms behind an increasing turbopause height during summer are not fully agreed upon, but possible explanations may include changes in dynamics. Hoffmann et al. (2011) found an increasing trend of mesospheric GWs at a midlatitude station during summer over the last two decades. One theory is that a trend in GW activity may influence the turbopause height trend.

5.3. Critical assessment of own work

5.3.1. Paper 1

In addition to the results summarised in Section 5.1.1, we presented daily temperatures retrieved from OH*(6-2) together with 10 hPa stratospheric reanalysis temperatures provided through the Modern-Era Retrospective-analysis for Research and Applications (MERRA) project (Rienecker et al., 2011) (see Figure 2, *Paper 1*). The original idea of including MERRA temperatures in the plot was to investigate the hypothesis of whether SSWs are preceded by a decrease in OH* temperatures, as reported in literature (e.g. Hoffmann et al., 2007; Walterscheid et al., 2000). However, by looking at measurements from only one station, at one height, we do not get the whole picture. From the plot it is hard to find clear signatures of mesospheric cooling preceding SSWs. This is, however, not equivalent to that the polar mesosphere did not cool. The cooling could have been confined to a region further down in the mesosphere. Also, SSWs may affect the mesospheric circulation with a longitudinal and latitudinal dependence (e.g. Hoffmann et al., 2007). Longyearbyen may have been located outside of the affected sector for some of the SSW events. In *Paper 1*, we did not elaborate further on this topic. The reason for this is that in order to investigate this particular hypothesis, it is necessary to look at more data than we did, e.g. temperature and wind measurements from additional stations and at different heights.

For some reason, no attempts were made to explain the seasonal variation found in the dataset, other than stating that the temperature minimum, noticeable in the transition between December and January, is consistent with previous investigations of the dataset (Myrabø, 1986). Myrabø (1986) ex-

plained the temperature minimum in terms of changes in the GW activity and in the circulation, temperature and transport in the underlying atmosphere. Myrabø analysed four seasons of hydroxyl airglow temperatures from Longyearbyen and observed the temperature minimum regardless of SSW occurrence.

5.3.2. Paper 2

The uncertainties of the results obtained are large, for both the solar response coefficient and the trend. In *Paper 4*, we applied criteria from Weatherhead et al. (1998) and Tiao et al. (1990) in order to determine if the trend we found could be considered detectable and significantly non-zero. We did not perform the same procedure in *Paper 2*. Following the criteria, the Longyearbyen OH*(6-2) airglow temperature trend cannot be considered neither significantly non-zero nor detectable. In fact, according to the formulation (Weatherhead et al., 1998, Eq. 3) the number of years required for a detectable trend is 180. The small magnitude of the trend and the large standard deviation of the time series explain why this number is so large.

Weatherhead et al. (1998) stress the importance of accounting for level shifts in the data, caused when e.g. instrument location changes, or when an instrument is modified. The Ebert-Fastie spectrometer was moved from the Auroral Station in Adventdalen to the Kjell Henriksen Observatory in 2007, and it has gone through upgrades including changing counter cards, high voltage supplies, pulse amplifier/discriminator, photomultiplier tube and cooler. Even though upgrades are inevitable for a spectrometer operating over a time period of more than 30 years, such operations will affect the performance of the instrument. Ignoring them can result in artificial trends in the data not representative for the actual temperature change. Often one does not know the magnitude of such level shifts, but knowing the time for the occurring level shifts enables us to account for them. Level shifts result in increased variance, and hence a lengthening of the time required for a detectable trend. Level shifts were not accounted for in *Paper 2*, and we do not know the effects of level shifts on the trend.

The number of observing days, which are days where we have minimum three hours of "good" data, varies a lot from one season to another. One anonymous referee suggested to perform a so-called bootstrap analysis, using randomised data points. The principle behind a bootstrap analysis is to select the same number of data points from each season, repeat the randomisation many times and then plot the distribution of the means or medians per season. We did not perform this procedure in the trend analysis. However, it would be useful to do this and check if it would change the statistics and conclusions significantly.

Using temperatures obtained from airglow intensities results in a masking of certain atmospheric conditions. For instance will spectra obtained during periods of strong aurora or thick tropospheric cloud cover be classified as "poor" and filtered out of the dataset. Avoiding this is not possible when using airglow temperatures, but one option is to compare the airglow temperatures with e.g. temperatures obtained from the Nippon/Norway Svalbard Meteor Radar located in Adventdalen.

5.3.3. Paper 3

The increasing turbopause height during summer is commensurate with decreasing atomic oxygen concentrations, as proposed by Oliver et al. (2014). A suggestion for making a more direct geographic comparison would be to e.g. analyse the trend in atomic oxygen retrieved from the SCIAMACHY instrument on board the Envisat satellite. SCIAMACHY provided atomic oxygen concentration profiles from the MLT region from 50°S to 75°N from 2002 to 2012, covering a large part of the turbopause height dataset.

5.3.4. Paper 4

The meteor radar temperature dataset does not cover a complete solar cycle, and hence it is not long enough for including the solar response in the trend. We had to go through many steps to calibrate the temperatures with respect to Aura MLS temperatures, which are associated with considerable uncertainties at mesopause heights.

We proposed explanations for the seasonal variation of temperatures, involving GW and PW activity affecting atmospheric circulation. However, we did not include any actual analysis of GWs or PWs from observations. It is possible to extract PW activity from meridional wind anomalies using SuperDARN radars, as conducted by Stray et al. (2014). It is not possible to extract GW momentum flux with the instrumentation we have available in Tromsø.

6. Concluding remarks

In this thesis, we have worked towards a better understanding of processes responsible for temperature variability in the polar mesopause region. We have also investigated trends in temperature obtained from this region and in turbopause height. In order to investigate these main objectives, we have utilised data from two high-latitude stations: Tromsø (70°N, 19°E) and Longyearbyen (78°N, 16°E). A 1 m Ebert-Fastie spectrometer located at the Kjell Henriksen Observatory in Longyearbyen has been providing hydroxyl airglow temperatures for more than 30 years, making the Longyearbyen OH*(6-2) temperature record one of the longest time series of hydroxyl airglow winter temperatures in the world. Most of the ground-based measurements of the upper atmosphere from mainland Norway are conducted from Ramfjordmoen research station near Tromsø. Ramfjordmoen houses, amongst others, a medium-frequency radar and a meteor radar. The Nippon/Norway Tromsø Meteor Radar has been providing neutral temperatures from the mesopause region since 2003 by measuring decay times of echoes from ionised meteor trails. The great advantage of the meteor radar is its ability to conduct measurements of meteor echo decay times 24 hours a day, all year round, and the temperature record has very few data gaps. The medium-frequency radar has been operational for more than 40 years and has provided turbulent energy dissipation rates, which can be used to derive turbopause height, since 2000.

Seasonal variability of polar mesopause region temperatures obtained from the Ebert-Fastie spectrometer and the NTMR radar was investigated, and we found that the two datasets experience different seasonal variability. The Longyearbyen dataset experience local temperature maxima in mid-January and mid-February, as well as a minimum in the transition between December and January. In the NTMR dataset we identified periodic variations with periods ranging from 9 days to a year and local temperature enhancements after spring equinox and summer solstice. Even though solar variability and energetic particles precipitating in this region may have an effect on the temperature variability, the largest contributors are dynamic processes. Seasonal variation of temperature, and variability within this variation, correspond well to characteristic behaviour of the large-scale circulation in the middle atmosphere and corresponding wave activity. The fact that the winter climatology differs between Longyearbyen and Tromsø suggests that differences in local orographic forcing may play a large role.

6. Concluding remarks

The OH*(6-2) airglow winter temperature trend and the annual and summer NTMR temperature trends were estimated to be near-zero or slightly negative. The estimated NTMR winter trend was negative, $(-11.6 \pm 4.1)\,\mathrm{K\,decade^{-1}}$. The temperature trends obtained in this PhD project are in line with results from other studies on MLT temperatures at mid- and high-latitudes, as well as model studies (e.g. Beig, 2011; French and Klekociuk, 2011; Offermann et al., 2010; Schmidt et al., 2006), indicating zero or slightly negative trends. Increasing greenhouse gas emissions, which may lead to changes in dynamics, is proposed as the main driver behind a cooling of the middle atmosphere (e.g. Akmaev and Fomichev, 2000). The stronger cooling trend found in winter for the NTMR dataset is also found in other studies. This has in other studies been explained by effects associated with CO_2 radiative forcing (Fomichev et al., 2007; Schmidt et al., 2006).

The response on mesopause region temperatures to solar variability was investigated for the Longyearbyen OH*(6-2) airglow temperatures, but not for the NTMR temperatures, due to that the time series was shorter than the corresponding solar cycle. The solar response coefficient, decoupled from the multivariate regression analysis performed on the OH* temperatures, was $(3.6 \pm 4.0)\,\mathrm{K/100\,SFU}$. The magnitude of the solar response coefficient is on the same level as results obtained from other mid-latitude and high-latitude sites (French and Klekociuk, 2011; Offermann et al., 2010; She and Krueger, 2004).

The large temperature variability, in both OH* airglow temperatures from Longyearbyen and meteor radar temperatures from Tromsø, makes trend assessments challenging. The variability strongly influences the precision of trend estimates, which again determines the number of years required to detect a trend of a given magnitude. Level shifts in the data, which are present in the Longyearbyen OH* airglow dataset, further lengthen the time required for a detectable trend. Neither the winter trend in OH* airglow temperatures from Longyearbyen nor the overall trend in Tromsø meteor radar temperatures is detectable. The negative NTMR winter trend is significantly non-zero and detectable, according to criteria in Tiao et al. (1990) and Weatherhead et al. (1998).

An increase in turbopause height of $(1.6 \pm 0.3)\,\mathrm{km\,decade^{-1}}$ over Tromsø is evident from 1999 to 2015 for summer, whereas for winter the turbopause height has not changed significantly. Increasing turbopause height during summer is commensurate with decreasing atomic oxygen concentrations over the same time period, as shown by Oliver et al. (2014). An increasing trend in GW activity during summer, found by e.g. Hoffmann et al. (2011), is a possible explanation for our findings.

The location of the turbopause is important for transport of atmospheric constituents, both upwards and downwards. Constituents produced in the

lower atmosphere are transported upwards due to turbulence, and the higher the turbopause, the higher up into the middle atmosphere the constituents are transported. Atomic oxygen is an example of an atmospheric component whose downward transport into the mesosphere is affected by turbopause height. Atomic oxygen is produced by dissociation of molecular oxygen in the ionosphere. When the turbopause is located at a low level, e.g. during summer, it may be below the lower limit of atomic oxygen production, and thus downward transport to the mesosphere does not occur. Transport of atomic oxygen into this region is important for ozone chemistry and hence hydroxyl airglow chemistry.

Whether or not the change in turbopause height over Tromsø affects the transport of atomic oxygen necessary for influencing airglow chemistry is difficult to investigate further. Airglow measurements have not been conducted from Tromsø during the same time period as turbulent energy dissipation rates have been measured by the MF radar. Hydroxyl airglow temperatures have been measured during winter at Arctic Lidar Observatory for Middle Atmosphere Research (ALOMAR) in Andøya (69°N, 16°E) since 2010. Since it is during summer that we have found a change in the turbopause height, it is difficult to investigate the effects of this on Arctic airglow measurements, due to the light conditions during Arctic summer.

7. Future perspectives

The work done in this PhD thesis opens up possibilities for new projects. As previously mentioned, airglow intensity is directly proportional to atomic oxygen concentration. Atomic oxygen concentration is measured by e.g. SCIA-MACHY (between 50°S and 75°N) and could give important insights into both the evolution of turbopause height and its influence on airglow dynamics at high latitudes. A useful approach would be to examine the trend in atomic oxygen concentration measured by SCIAMACHY and compare with the trend in turbopause height, as well as results obtained by Oliver et al. (2014).

Regarding airglow variability over Longyearbyen, a lot is still undone. Topics that need further attention are related to the variability of the OH* layer altitude and number density with the diurnal cycle and in the context of e.g. GWs and SSWs, as well as long-term changes in the layer. Using ground-based measurements of OH* airglow temperatures from Longyearbyen in combination with satellite measurements of peak altitudes of the OH* layer, derived from integrated volume emission rates, would be valuable in this context. The new SuperDARN radar in Longyearbyen, operative since 2015, may also be used for studying gravity waves.

Also, identifying periodic oscillations in the OH* airglow dataset, as well as temperatures derived from the Nippon/Norway Svalbard Meteor Radar in Longyearbyen, would shed light on dynamics affecting the airglow layer over Svalbard. The results should be compared with the results obtained in *Paper 4*.

Other future projects could involve monitoring effects of energetic particle precipitation on mesopause temperatures obtained at high latitudes, using e.g. geomagnetic indices or particle fluxes measured by POES satellites.

Bibliography

Adler-Golden, S. (1997). "Kinetic parameters for OH nightglow modeling consistent with recent laboratory measurements". In: *Journal of Geophysical Research: Space Physics* 102.A9, pp. 19969–19976. DOI: 10.1029/97JA01622.

Akmaev, R. A. and V. I. Fomichev (1998). "Cooling of the mesosphere and lower thermosphere due to doubling of CO_2". In: *Annales Geophysicae* 16.11, pp. 1501–1512. DOI: 10.1007/s00585-998-1501-z.

Akmaev, R. A. and V. I. Fomichev (2000). "A model estimate of cooling in the mesosphere and lower thermosphere due to the CO_2 increase over the last 3–4 decades". In: *Geophysical Research Letters* 27.14, pp. 2113–2116. DOI: 10.1029/1999GL011333.

Andrews, D. G., J. R. Holton, and C. B. Leovy (1987). *Middle atmosphere dynamics*. International geophysics series 40. Academic press.

Baker, D. J. and A. T. Stair (1988). "Rocket measurements of the altitude distributions of the hydroxyl airglow". In: *Physica Scripta* 37, pp. 611–622. DOI: 10.1088/0031-8949/37/4/021.

Ballinger, A. P., P. B. Chilson, R. D. Palmer, and N. J. Mitchell (2008). "On the validity of the ambipolar diffusion assumption in the polar mesopause region". In: *Annales Geophysicae* 26.11, pp. 3439–3443. DOI: 10.5194/angeo-26-3439-2008.

Bates, D. R. and M. Nicolet (1950). "The photochemistry of atmospheric water vapor". In: *Journal of Geophysical Research* 55.3, pp. 301–327. DOI: 10.1029/JZ055i003p00301.

Beig, G. (2011). "Long-term trends in the temperature of the mesosphere/lower thermosphere region: 1. Anthropogenic influences". In: *Journal of Geophysical Research: Space Physics* 116.A2. DOI: 10.1029/2011JA016646.

Beig, G., J. Scheer, M. G. Mlynczak, and P. Keckhut (2008). "Overview of the temperature response in the mesosphere and lower thermosphere to solar activity". In: *Reviews of Geophysics* 46.3. DOI: 10.1029/2007RG000236.

Bittner, M., D. Offermann, and H. H. Graef (2000). "Mesopause temperature variability above a midlatitude station in Europe". In: *Journal of Geophysical Research: Atmospheres* 105.D2, pp. 2045–2058. DOI: 10.1029/1999JD900307.

Bibliography

Blamont, J.-E. (1963). "Turbulence in atmospheric motions between 90 and 130 km of altitude". In: *Planetary and Space Science* 10, pp. 89–101. DOI: 10.1016/0032-0633(63)90010-2.

Booker, J. R. and F. P. Bretherton (1967). "The critical layer for internal gravity waves in a shear flow". In: *Journal of Fluid Mechanics* 27.03, pp. 513–539. DOI: 10.1017/S0022112067000515.

Brasseur, G. and M. Nicolet (1973). "Chemospheric processes of nitric oxide in the mesosphere and stratosphere". In: *Planetary and Space Science* 21.6, pp. 939–961. DOI: 10.1016/0032-0633(73)90141-4.

Brekke, A., O. Holt, P. H. G. Dickinson, M. Friedrich, T. Hansen, P. Stauning, and E. V. Thrane (1985). "Development of D-region electron and ion densities under various auroral conditions during the Energy Budget Campaign (EBC)". In: *Journal of Atmospheric and Terrestrial Physics* 47.1, pp. 101–121. DOI: 10.1016/0021-9169(85)90127-8.

Brewer, A. W. (1949). "Evidence for a world circulation provided by the measurements of helium and water vapour distribution in the stratosphere". In: *Quarterly Journal of the Royal Meteorological Society* 75.326, pp. 351–363. DOI: 10.1002/qj.49707532603.

Briggs, B. H. (1980). "Radar observations of atmospheric winds and turbulence: A comparison of techniques". In: *Journal of Atmospheric and Terrestrial Physics* 42.9, pp. 823–833. DOI: 10.1016/0021-9169(80)90086-0.

Cervera, M. A. and I. M. Reid (2000). "Comparison of atmospheric parameters derived from meteor observations with CIRA". In: *Radio Science* 35.3, pp. 833–843. DOI: 10.1029/1999RS002226.

Chamberlain, J. W. (1961). *Physics of the Aurora and Airglow*. Academic press, New York.

Chamberlain, J. W. and F. L. Roesler (1955). "The OH Bands in the Infrared Airglow". In: *The Astrophysical Journal* 121, p. 541. DOI: 10.1086/146015.

Chapman, S. (1931). "Bakerian Lecture. Some phenomena of the upper atmosphere". In: *Proceedings of the Royal Society of London. Series A, Containing Papers of a Mathematical and Physical Character* 132.820, pp. 353–374.

Charney, J. G. and P. G. Drazin (1961). "Propagation of planetary-scale disturbances from the lower into the upper atmosphere". In: *Journal of Geophysical Research* 66.1, pp. 83–109. DOI: 10.1029/JZ066i001p00083.

Cosby, P. C. and T. G. Slanger (2007). "OH spectroscopy and chemistry investigated with astronomical sky spectra". In: *Canadian Journal of Physics* 85.2, pp. 77–99. DOI: 10.1139/p06-088.

Czechowsky, P., I. M. Reid, and R. Rüster (1988). "VHF radar measurements of the aspect sensitivity of the summer polar mesopause echoes over

Andenes (69°N,16°E), Norway". In: *Geophysical Research Letters* 15.11, pp. 1259–1262. DOI: 10.1029/GL015i011p01259.

Danilov, A. D., U. A. Kalgin, and A. A. Pokhunkov (1979). "Variation of the turbopause level in the polar regions". In: *Space Research XIX* 173.

Dickinson, R. E. (1978). "Rossby waves–long-period oscillations of oceans and atmospheres". In: *Annual Review of Fluid Mechanics* 10.1, pp. 159–195. DOI: 10.1146/annurev.fl.10.010178.001111.

Dobson, G. M. B. (1956). "Origin and distribution of the polyatomic molecules in the atmosphere". In: *Proceedings of the Royal Society of London. Series A, Mathematical and Physical Sciences* 236.1205, pp. 187–193.

Dowdy, A. J., R. A. Vincent, D. J. Murphy, M. Tsutsumi, D. M. Riggin, and M. J. Jarvis (2004). "The large-scale dynamics of the mesosphere–lower thermosphere during the Southern Hemisphere stratospheric warming of 2002". In: *Geophysical Research Letters* 31.14. DOI: 10.1029/2004GL020282.

Dunkerton, T. (1978). "On the mean meridional mass motions of the stratosphere and mesosphere". In: *Journal of the Atmospheric Sciences* 35.12, pp. 2325–2333. DOI: 10.1175/1520-0469(1978)035<2325:OTMMMM>2.0.CO;2.

Dunkerton, T. J. (1991). "LIMS (Limb Infrared Monitor of the Stratosphere) observation of traveling planetary waves and potential vorticity advection in the stratosphere and mesosphere". In: *Journal of Geophysical Research: Atmospheres* 96.D2, pp. 2813–2834. DOI: 10.1029/90JD02340.

Dyrland, M. E., F. J. Mulligan, C. M. Hall, F. Sigernes, M. Tsutsumi, and C. S. Deehr (2010). "Response of OH airglow temperatures to neutral air dynamics at 78°N, 16°E during the anomalous 2003–2004 winter". In: *Journal of Geophysical Research* 115 (D07103). DOI: 10.1029/2009JD012726.

Dyrland, M. E. and F. Sigernes (2007). "An update on the hydroxyl airglow temperature record from the Auroral Station in Adventdalen, Svalbard (1980–2005)". In: *Canadian Journal of Physics* 85.2, pp. 143–151. DOI: 10.1139/p07-040.

Dyrud, L. P., M. M. Oppenheim, and A. F. vom Endt (2001). "The anomalous diffusion of meteor trails". In: *Geophysical Research Letters* 28.14, pp. 2775–2778. DOI: 10.1029/2000GL012749.

Ecklund, W. L. and B. B. Balsley (1981). "Long-term observations of the Arctic mesosphere with the MST radar at Poker Flat, Alaska". In: *Journal of Geophysical Research: Space Physics* 86.A9, pp. 7775–7780. DOI: 10.1029/JA086iA09p07775.

Eliassen, A. and E. Palm (1961). "On the transfer of energy in stationary mountain waves". In: *Geofysiske Publikasjoner* 22, pp. 1–23.

Espy, P. J. and J. Stegman (2002). "Trends and variability of mesospheric temperature at high-latitudes". In: *Physics and Chemistry of the Earth, Parts A/B/C* 27.6, pp. 543–553. DOI: `10.1016/S1474-7065(02)00036-0`.

Fels, S. B. (1985). "Radiative-dynamical interactions in the middle atmosphere". In: *Advances in Geophysics* 28, pp. 277–300. DOI: `10.1016/S0065-2687(08)60227-7`.

Fleming, E. L., S. Chandra, J. J. Barnett, and M. Corney (1990). "Zonal mean temperature, pressure, zonal wind and geopotential height as functions of latitude". In: *Advances in Space Research* 10.12, pp. 11–59. DOI: `10.1016/0273-1177(90)90386-E`.

Fomichev, V. I., A. I. Jonsson, J. De Grandpre, S. R. Beagley, C. McLandress, K. Semeniuk, and T. G. Shepherd (2007). "Response of the middle atmosphere to CO_2 doubling: Results from the Canadian Middle Atmosphere Model". In: *Journal of Climate* 20.7, pp. 1121–1144. DOI: `10.1175/JCLI4030.1`.

Forbes, J. M., A. H. Manson, R. A. Vincent, G. J. Fraser, F. Vial, R. Wand, S. K. Avery, R. R. Clark, R. Johnson, R. Roper, R. Schminder, T. Tsuda, and E. S. Kazimirovsky (1994). "Semidiurnal tide in the 80–150 km region: an assimilative data analysis". In: *Journal of Atmospheric and Terrestrial Physics* 56.10, pp. 1237–1249. DOI: `10.1016/0021-9169(94)90062-0`.

French, W. J. R. and G. B. Burns (2004). "The influence of large-scale oscillations on long-term trend assessment in hydroxyl temperatures over Davis, Antarctica". In: *Journal of Atmospheric and Solar-Terrestrial Physics* 66.6, pp. 493–506. DOI: `10.1016/j.jastp.2004.01.027`.

French, W. J. R., G. B. Burns, K. Finlayson, P. A. Greet, R. P. Lowe, and P. F. B. Williams (2000). "Hydroxyl (6-2) airglow emission intensity ratios for rotational temperature determination". In: *Annales Geophysicae* 18.10, pp. 1293–1303. DOI: `10.1007/s00585-000-1293-2`.

French, W. J. R. and A. R. Klekociuk (2011). "Long-term trends in Antarctic winter hydroxyl temperatures". In: *Journal of Geophysical Research: Atmospheres* 116.D4. DOI: `10.1029/2011JD015731`.

Fritts, D. C. (1984). "Gravity wave saturation in the middle atmosphere: A review of theory and observations". In: *Reviews of Geophysics* 22.3, pp. 275–308. DOI: `10.1029/RG022i003p00275`.

Fritts, D. C. and M. J. Alexander (2003). "Gravity wave dynamics and effects in the middle atmosphere". In: *Reviews of Geophysics* 41.1. DOI: `10.1029/2001RG000106`.

Fukao, S., M. D. Yamanaka, N. Ao, W. K. Hocking, T. Sato, M. Yamamoto, T. Nakamura, T. Tsuda, and S. Kato (1994). "Seasonal variability of vertical eddy diffusivity in the middle atmosphere: 1. Three-year observations by the middle and upper atmosphere radar". In: *Journal of Geophysical Research: Atmospheres* 99.D9, pp. 18973–18987. DOI: `10.1029/94JD00911`.

Garcia, R. R. and S. Solomon (1985). "The effect of breaking gravity waves on the dynamics and chemical composition of the mesosphere and lower thermosphere". In: *Journal of Geophysical Research: Atmospheres* 90.D2, pp. 3850–3868. DOI: 10.1029/JD090iD02p03850.

Gibbs, J. W. (1902). *Elementary principles in statistical mechanics*. Scribner's sons, New York.

Grygalashvyly, Mykhaylo (2015). "Several notes on the OH* layer". In: *Annales Geophysicae* 33, pp. 923–930. DOI: 10.5194/angeo-33-923-2015.

Hall, C. (2001). "The Ramfjordmoen MF radar (69°N, 19°E): application development 1990–2000". In: *Journal of Atmospheric and Solar-Terrestrial Physics* 63.2, pp. 171–179. DOI: 10.1016/S1364-6826(00)00144-9.

Hall, C. M., T. Aso, M. Tsutsumi, J. Höffner, F. Sigernes, and D. A. Holdsworth (2006). "Neutral air temperatures at 90 km and 70°N and 78°N". In: *Journal of Geophysical Research: Atmospheres* 111.D14105. DOI: 10.1029/2005JD006794.

Hall, C. M., T. Aso, M. Tsutsumi, S. Nozawa, A. H. Manson, and C. E. Meek (2005a). "A comparison of mesosphere and lower thermosphere neutral winds as determined by meteor and medium-frequency radar at 70°N". In: *Radio Science* 40.4. DOI: 10.1029/2004RS003102.

Hall, C. M., T. Aso, M. Tsutsumi, S. Nozawa, A. H. Manson, and C. E. Meek (2005b). "Letter to the Editor: Testing the hypothesis of the influence of neutral turbulence on the deduction of ambipolar diffusivities from meteor trail expansion". In: *Annales Geophysicae* 23, pp. 1071–1073. DOI: 10.5194/angeo-23-1071-2005.

Hall, C. M., A. Brekke, A. H. Manson, C. E. Meek, and S. Nozawa (2007). "Trends in mesospheric turbulence at 70°N". In: *Atmospheric Science Letters* 8.3, pp. 80–84. DOI: 10.1002/asl.156.

Hall, C. M., A. H. Manson, and C. E. Meek (1998a). "Seasonal variation of the turbopause: One year of turbulence investigation at 69°N by the joint University of Tromsø/University of Saskatchewan MF radar". In: *Journal of Geophysical Research: Atmospheres* 103.D22, pp. 28769–28773. DOI: 10.1029/1998JD200002.

Hall, C. M., C. E. Meek, and A. H. Manson (1998b). "Turbulent energy dissipation rates from the University of Tromsø/University of Saskatchewan MF radar". In: *Journal of Atmospheric and Solar-Terrestrial Physics* 60.4, pp. 437–440. DOI: 10.1016/S1364-6826(97)00124-7.

Hall, C. M., C. E. Meek, A. H. Manson, and S. Nozawa (2008). "Turbopause determination, climatology, and climatic trends using medium frequency radars at 52°N and 70°N". In: *Journal of Geophysical Research: Atmospheres* 113.D13. DOI: 10.1029/2008JD009938.

Hall, C. M. and M. Tsutsumi (2013). "Changes in mesospheric dynamics at 78°N, 16°E and 70°N, 19°E: 2001–2012". In: *Journal of Geophysical Research: Atmospheres* 118.7, pp. 2689–2701. DOI: 10.1002/jgrd.50268.

Hargreaves, J. K. and A. Brekke (1981). "Application of the Ramfjordmoen partial reflection experiment to the study of auroral precipitation events". In: *Journal of Atmospheric and Terrestrial Physics* 43.10, pp. 1093–1106. DOI: 10.1016/0021-9169(81)90024-6.

Herzberg, G. (1950). *Molecular spectra and molecular structure. Vol 1: Spectra of diatomic molecules.* Second edition. Van Nostrand Reinhold, New York.

Hill, E. and J. H. Van Vleck (1928). "On the quantum mechanics of the rotational distortion of multiplets in molecular spectra". In: *Physical Review* 32 (2), pp. 250–272. DOI: 10.1103/PhysRev.32.250.

Hines, C. O. (1960). "Internal atmospheric gravity waves at ionospheric heights". In: *Canadian Journal of Physics* 38.11, pp. 1441–1481. DOI: 10.1139/p60-150.

Hocking, W. K. (1983). "On the extraction of atmospheric turbulence parameters from radar backscatter Doppler spectra—I. Theory". In: *Journal of Atmospheric and Terrestrial Physics* 45.2-3, pp. 89–102. DOI: 10.1016/S0021-9169(83)80013-0.

Hocking, W. K. (1985). "Measurement of turbulent energy dissipation rates in the middle atmosphere by radar techniques: A review". In: *Radio Science* 20.6, pp. 1403–1422. DOI: 10.1029/RS020i006p01403.

Hocking, W. K. (1987). "Turbulence in the region 80–120 km". In: *Advances in Space Research* 7.10, pp. 10171–10181. DOI: 10.1016/0273-1177(87)90090-1.

Hocking, W. K., T. Thayaparan, and J. Jones (1997). "Meteor decay times and their use in determining a diagnostic mesospheric temperature-pressure parameter: Methodology and one year of data". In: *Geophysical Research Letters* 24.23, pp. 2977–2980. DOI: 10.1029/97GL03048.

Hodges, R. R. (1967). "Generation of turbulence in the upper atmosphere by internal gravity waves". In: *Journal of Geophysical Research* 72.13, pp. 3455–3458. DOI: 10.1029/JZ072i013p03455.

Hoffmann, P., E. Becker, W. Singer, and M. Placke (2010). "Seasonal variation of mesospheric waves at northern middle and high latitudes". In: *Journal of Atmospheric and Solar-Terrestrial Physics* 72.14, pp. 1068–1079. DOI: 10.1016/j.jastp.2010.07.002.

Hoffmann, P., M. Rapp, W. Singer, and D. Keuer (2011). "Trends of mesospheric gravity waves at northern middle latitudes during summer". In: *Journal of Geophysical Research: Atmospheres* 116.D4. DOI: 10.1029/2011JD015717.

Hoffmann, P., W. Singer, D. Keuer, W. K. Hocking, M. Kunze, and Y. Murayama (2007). "Latitudinal and longitudinal variability of mesospheric

winds and temperatures during stratospheric warming events". In: *Journal of Atmospheric and Solar-Terrestrial Physics* 69.17, pp. 2355–2366. DOI: 10.1016/j.jastp.2007.06.010.

Holdsworth, D. A., R. J. Morris, D. J. Murphy, I. M. Reid, G. B. Burns, and W. J. R. French (2006). "Antarctic mesospheric temperature estimation using the Davis mesosphere-stratosphere-troposphere radar". In: *Journal of Geophysical Research: Atmospheres* 111.D5. DOI: 10.1029/2005JD006589.

Holton, J. R. (1983). "The influence of gravity wave breaking on the general circulation of the middle atmosphere". In: *Journal of the Atmospheric Sciences* 40.10, pp. 2497–2507. DOI: 10.1175/1520-0469(1983)040<2497:TIOGWB>2.0.CO;2.

Holton, J. R. (2004). *An introduction to dynamic meteorology*. Fourth edition. International geophysics series Vol. 1. Elsevier Academic press. ISBN: 9780123540157.

Holton, J. R. and R. S. Lindzen (1972). "An updated theory for the quasi-biennial cycle of the tropical stratosphere". In: *Journal of the Atmospheric Sciences* 29.6, pp. 1076–1080. DOI: 10.1175/1520-0469(1972)029<1076:AUTFTQ>2.0.CO;2.

Holton, J. R. and H.-C. Tan (1980). "The influence of the equatorial quasi-biennial oscillation on the global circulation at 50 mb". In: *Journal of the Atmospheric Sciences* 37.10, pp. 2200–2208. DOI: 10.1175/1520-0469(1980)037<2200:TIOTEQ>2.0.CO;2.

Hoppe, U.-P., C. Hall, and J. Röttger (1988). "First observations of summer polar mesospheric backscatter with a 224 MHz radar". In: *Geophysical Research letters* 15.1, pp. 28–31. DOI: 10.1029/GL015i001p00028.

Jones, J. (1975). "On the decay of underdense radio meteor echoes". In: *Monthly Notices of the Royal Astronomical Society* 173.3, pp. 637–647. DOI: 10.1093/mnras/173.3.637.

Kaiser, T. R. (1953). "Radio echo studies of meteor ionization". In: *Advances in Physics* 2.8, pp. 495–544. DOI: 10.1080/00018735300101282.

Kolmogorov, A. N. (1941). "The local structure of turbulence in incompressible viscous fluid for very large Reynolds numbers". In: *Doklady Akademiia Nauk SSSR* 30, pp. 299–303.

Kovalev, D. V., A. P. Smirnov, and Y. S. Dimant (2008). "Annales Geophysicae". In: 26.9, pp. 2853–2870. DOI: 10.5194/angeo-26-2853-2008.

Krassovsky, V. I., N. N. Shefov, and V. I. Yarin (1962). "Atlas of the airglow spectrum 3000–12400 Å". In: *Planetary and Space Science* 9.12, pp. 883–915. DOI: 10.1016/0032-0633(62)90008-9.

Kurihara, J., Y. Ogawa, S. Oyama, S. Nozawa, M. Tsutsumi, C. M. Hall, Y. Tomikawa, and R. Fujii (2010). "Links between a stratospheric sudden warming and thermal structures and dynamics in the high-latitude meso-

sphere, lower thermosphere, and ionosphere". In: *Geophysical Research Letters* 37.13. DOI: 10.1029/2010GL043643.

Labitzke, K. (1981). "Stratospheric-mesospheric midwinter disturbances: A summary of observed characteristics". In: *Journal of Geophysical Research: Oceans* 86.C10, pp. 9665–9678. DOI: 10.1029/JC086iC10p09665.

Labitzke, K. and B. Naujokat (2000). "The lower Arctic stratosphere in winter since 1952". In: *Sparc Newsletter* 15, pp. 11–14.

Lean, J. L. and A. Skumanich (1983). "Variability of the Lyman alpha flux with solar activity". In: *Journal of Geophysical Research: Space Physics* 88.A7, pp. 5751–5759. DOI: 10.1029/JA088iA07p05751.

Lehmacher, G. A., T. D. Scott, M. F. Larsen, S. G. Bilén, C. L. Croskey, J. D. Mitchell, M. Rapp, F.-J. Lübken, and R. L. Collins (2011). "The Turbopause experiment: atmospheric stability and turbulent structure spanning the turbopause altitude". In: *Annales Geophysicae* 29, pp. 2327–2339. DOI: 10.5194/angeo-29-2327-2011.

Lindzen, R. S. (1981). "Turbulence and stress owing to gravity wave and tidal breakdown". In: *Journal of Geophysical Research: Oceans* 86.C10, pp. 9707–9714. DOI: 10.1029/JC086iC10p09707.

Lindzen, R. S. and J. R. Holton (1968). "A theory of the quasi-biennial oscillation". In: *Journal of the Atmospheric Sciences* 25.6, pp. 1095–1107. DOI: 10.1175/1520-0469(1968)025<1095:ATOTQB>2.0.CO;2.

Liu, G. and G. G. Shepherd (2006). "An empirical model for the altitude of the OH nightglow emission". In: *Geophysical Research Letters* 33 (L09805). DOI: 10.1029/2005GL025297.

Liu, G., G. G. Shepherd, and R. G. Roble (2008). "Seasonal variations of the nighttime O(^{1}S) and OH airglow emission rates at mid-to-high latitudes in the context of the large-scale circulation". In: *Journal of Geophysical Research: Space Physics* 113.A06302. DOI: 10.1029/2007JA012854.

Lomb, N. R. (1976). "Least-squares frequency analysis of unequally spaced data". In: *Astrophysics and Space Science* 39.2, pp. 447–462. DOI: 10.1007/BF00648343.

Lübken, F.-J. (1999). "Thermal structure of the Arctic summer mesosphere". In: *Journal of Geophysical Research: Atmospheres* 104.D8, pp. 9135–9149. DOI: 10.1029/1999JD900076.

Lübken, F.-J. and U. von Zahn (1991). "Thermal structure of the mesopause region at polar latitudes". In: *Journal of Geophysical Research: Atmospheres* 96.D11, pp. 20841–20857. DOI: 10.1029/91JD02018.

Luo, Y., A. H. Manson, C. E. Meek, C. K. Meyer, M. D. Burrage, D. C. Fritts, C. M. Hall, W. K. Hocking, J. MacDougall, D. M. Riggin, and R. A. Vincent (2002). "The 16-day planetary waves: multi-MF radar observations from the arctic to equator and comparisons with the HRDI measurements

and the GSWM modelling results". In: *Annales Geophysicae* 20.5, pp. 691–709. DOI: `10.5194/angeo-20-691-2002`.

Manabe, S. and R. T. Wetherald (1975). "The effect of doubling the CO_2 concentration on the climate of a general circulation model". In: *Journal of Atmospheric Sciences* 32.1, pp. 3–15. DOI: `10.1175/1520-0469(1975) 032<0003:TEODTC>2.0.CO;2`.

Manson, A. H. and C. E. Meek (1991). "Climatologies of mean winds and tides observed by medium frequency radars at Tromsö (70°N) and Saskatoon (52°N) during 1987–1989". In: *Canadian Journal of Physics* 69.8-9, pp. 966–975. DOI: `10.1139/p91-152`.

Manson, A. H., C. E. Meek, A. Brekke, and J. Moen (1992). "Mesosphere and lower thermosphere (80–120 km) winds and tides from near Troms0 (70°N, 19°E): Comparisons between radars (MF, EISCAT, VHF) and rockets". In: *Journal of Atmospheric and Terrestrial Physics* 54.7, pp. 927–950. DOI: `10.1016/0021-9169(92)90059-T`.

Manson, A. H., C. E. Meek, C. Hall, W. K. Hocking, J. MacDougall, S. Franke, K. Igarashi, D. Riggin, D. C. Fritts, and R. A. Vincent (1999). "Gravity wave spectra, directions and wave interactions: Global MLT-MFR network". In: *Earth, Planets and Space* 51.7–8, pp. 543–562. DOI: `10.1186/BF03353214`.

Manson, A. H., C. E. Meek, T. L. Hansen, and T. Trondsen (1990a). "Dynamics of the upper middle atmosphere (80–110 km) at Tromsø (70°N) and Saskatoon (52°N), June–December 1987, using the Tromsø and Saskatoon MF radars". In: *Journal of Atmospheric and Terrestrial Physics* 52.10-11, pp. 971–980. DOI: `10.1016/0021-9169(90)90028-L`.

Manson, A. H., C. E. Meek, R. Schminder, D. Kürschner, R. R. Clark, H. G. Müller, R. A. Vincent, A. Phillips, G. J. Fraser, W. Singer, and E. S. Kazimirovsky (1990b). "Tidal winds from the MLT global radar network during the first LTCS campaign—September 1987". In: *Journal of Atmospheric and Terrestrial Physics* 52.3, pp. 175–183. DOI: `10.1016/0021-9169(90)90121-3`.

Matsuno, T. (1971). "A dynamical model of the stratospheric sudden warming". In: *Journal of the Atmospheric Sciences* 28.8, pp. 1479–1494. DOI: `10.1175/1520-0469(1971)028<1479:ADMOTS>2.0.CO;2`.

McDade, I. C. (1991). "The altitude dependence of the OH ($X^2 \Pi$) vibrational distribution in the nightglow: Some model expectations". In: *Planetary and Space Science* 39.7, pp. 1049–1057. DOI: `10.1016/0032-0633(91) 90112-N`.

McDaniel, E. W. and E. A. Mason (1973). *The mobility and diffusion of ions in gases.* John Wiley & Sons, Inc.

McKinley, D. W. R. (1961). *Meteor science and engineering.* McGraw-Hill, New York.

Meinel, A. B. (1950a). "OH emission bands in the spectrum of the night sky. I". In: *The Astrophysical Journal* 111, pp. 555–564. DOI: 10.1086/145296.

Meinel, A. B. (1950b). "OH emission bands in the spectrum of the night sky. II". In: *The Astrophysical Journal* 112, pp. 120–130. DOI: 10.1086/145321.

Mies, F. H. (1974). "Calculated vibrational transition probabilities of OH ($X^2 \Pi$)". In: *Journal of Molecular Spectroscopy* 53.2, pp. 150–188. DOI: 10.1016/0022-2852(74)90125-8.

Mulligan, F. J., M. E. Dyrland, F. Sigernes, and C. S. Deehr (2009). "Inferring hydroxyl layer peak heights from ground-based measurements of OH(6-2) band integrated emission rate at Longyearbyen (78°N, 16°E)". In: *Annales Geophysicae* 27.11, pp. 4197–4205. DOI: 10.5194/angeo-27-4197-2009.

Murgatroyd, R. J. and F. Singleton (1961). "Possible meridional circulations in the stratosphere and mesosphere". In: *Quarterly Journal of the Royal Meteorological Society* 87.372, pp. 125–135. DOI: 10.1002/qj.49708737202.

Myrabø, H. K. (1984). "Temperature variation at mesopause levels during winter solstice at 78°N". In: *Planetary and Space Science* 32.2, pp. 249–255. DOI: 10.1016/0032-0633(84)90159-4.

Myrabø, H. K. (1986). "Winter-season mesopause and lower thermosphere temperatures in the northern polar region". In: *Planetary and Space Science* 34.11, pp. 1023–1029. DOI: 10.1016/0032-0633(86)90012-7.

Myrabø, H. K., C. S. Deehr, and B. Lybekk (1984). "Polar cap OH airglow rotational temperatures at the mesopause during a stratospheric warming event". In: *Planetary and Space Science* 32.7, pp. 853–856. DOI: 10.1016/0032-0633(84)90009-6.

Newnham, D. A., P. J. Espy, M. A. Clilverd, C. J. Rodger, A. Seppälä, D. J. Maxfield, P. Hartogh, C. Straub, K. Holmén, and R. B. Horne (2013). "Observations of nitric oxide in the Antarctic middle atmosphere during recurrent geomagnetic storms". In: *Journal of Geophysical Research: Space Physics* 118.12, pp. 7874–7885. DOI: 10.1002/2013JA019056.

Noll, S., W. Kausch, S. Kimeswenger, S. Unterguggenberger, and A. M. Jones (2015). "OH populations and temperatures from simultaneous spectroscopic observations of 25 bands". In: *Atmospheric Chemistry and Physics* 15.7, pp. 3647–3669. DOI: 10.5194/acp-15-3647-2015.

Offermann, D., P. Hoffmann, P. Knieling, R. Koppmann, J. Oberheide, and W. Steinbrecht (2010). "Long-term trends and solar cycle variations of mesospheric temperature and dynamics". In: *Journal of Geophysical Research: Atmospheres* 115.D18. DOI: 10.1029/2009JD013363.

Offermann, D., M. Jarisch, H. Schmidt, J. Oberheide, K. U. Grossmann, O. Gusev, J. M. Russell III, and M. G. Mlynczak (2007). "The "wave

turbopause"". In: *Journal of Atmospheric and Solar-Terrestrial Physics* 69.17, pp. 2139–2158. DOI: 10.1016/j.jastp.2007.05.012.

Oliver, W. L., J. M. Holt, S.-R. Zhang, and L. P. Goncharenko (2014). "Long-term trends in thermospheric neutral temperature and density above Millstone Hill". In: *Journal of Geophysical Research: Space Physics* 119.9, pp. 7940–7946. DOI: 10.1002/2014JA020311.

Olivero, J. J. and G. E. Thomas (1986). "Climatology of polar mesospheric clouds". In: *Journal of the Atmospheric Sciences* 43.12, pp. 1263–1274. DOI: 10.1175/1520-0469(1986)043<1263:COPMC>2.0.CO;2.

Pendleton, W. R., P. J. Espy, and M. R. Hammond (1993). "Evidence for non-local-thermodynamic-equilibrium rotation in the OH nightglow". In: *Journal of Geophysical Research: Space Physics* 98.A7, pp. 11567–11579. DOI: 10.1029/93JA00740.

Picone, J. M., A. E. Hedin, D. P. Drob, and A. C. Aikin (2002). "NRLMSISE-00 empirical model of the atmosphere: Statistical comparisons and scientific issues". In: *Journal of Geophysical Research: Space Physics* 107.A12, SIA 15-1–SIA 15-16. DOI: 10.1029/2002JA009430.

Pierce, R. M. and S. E. Roark (2012). "Wind speed measurements of Doppler-shifted absorption lines using two-beam interferometry". In: *Applied Optics* 51.12, pp. 1853–1864. DOI: 10.1364/AO.51.001853.

Rapp, M. and F.-J. Lübken (2004). "Polar mesosphere summer echoes (PMSE): Review of observations and current understanding". In: *Atmospheric Chemistry and Physics* 4.11/12, pp. 2601–2633. DOI: 10.5194/acp-4-2601-2004.

Reynolds, O. (1894). "On the dynamical theory of incompressible viscous fluids and the determination of the criterion". In: *Proceedings of the Royal Society of London* 56, pp. 40–45. DOI: 10.1098/rspl.1894.0075.

Reynolds, W. C. (1987). "Fundamentals of turbulence for turbulence modeling and simulation". In: *Modern Theoretical and Experimental Approaches to Turbulent Flow Structure and its Modelling.*

Rienecker, M. M., M. J. Suarez, R. Gelaro, R. Todling, J. Bacmeister, E. Liu, M. G. Bosilovich, S. D. Schubert, L. Takacs, G.-K. Kim, S. Bloom, J. Chen, D. Collins, A. Conaty, A. Da Silva, W. Gu, J. Joiner, R. D. Koster, R. Lucchesi, A. Molod, T. Owens, S. Pawson, P. Pegion, C. R. Redder, R. Reichle, F. R. Robertson, A. G. Ruddick, M. Sienkiewicz, and J. Woollen (2011). "MERRA: NASA's modern-era retrospective analysis for research and applications". In: *Journal of Climate* 24.14, pp. 3624–3648. DOI: 10.1175/JCLI-D-11-00015.1.

Roble, R. G. and R. E. Dickinson (1989). "How will changes in carbon dioxide and methane modify the mean structure of the mesosphere and thermosphere?" In: *Geophysical Research Letters* 16.12, pp. 1441–1444. DOI: 10.1029/GL016i012p01441.

Rossby, C.-G. and collaborators (1939). "Relation between variations in the intensity of the zonal circulation of the atmosphere and the displacements of the semi-permanent centers of action". In: *Journal of Marine Research* 2.1, pp. 38–55.

Röttger, J., C. La Hoz, M. C. Kelley, U.-P. Hoppe, and C. Hall (1988). "The structure and dynamics of polar mesosphere summer echoes observed with the EISCAT 224 MHz radar". In: *Geophysical Research Letters* 15.12, pp. 1353–1356. DOI: 10.1029/GL015i012p01353.

Rubin, A. E. and J. N. Grossman (2010). "Meteorite and meteoroid: New comprehensive definitions". In: *Meteoritics & Planetary Science* 45.1, pp. 114–122. DOI: 10.1111/j.1945-5100.2009.01009.x.

Salby, M. L. (1981a). "Rossby normal modes in nonuniform background configurations. Part I: Simple fields". In: *Journal of the Atmospheric Sciences* 38.9, pp. 1803–1826. DOI: 10.1175/1520-0469(1981)038<1803: RNMINB>2.0.CO;2.

Salby, M. L. (1981b). "Rossby normal modes in nonuniform background configurations. Part II: Equinox and solstice conditions". In: *Journal of the Atmospheric Sciences* 38.9, pp. 1827–1840. DOI: 10.1175/1520-0469(1981) 038<1827:RNMINB>2.0.CO;2.

Scargle, J. D. (1982). "Studies in astronomical time series analysis. II. Statistical aspects of spectral analysis of unevenly spaced data". In: *The Astrophysical Journal* 263, pp. 835–853. DOI: 10.1086/160554.

Scheer, J. and E. R. Reisin (2007). "Is there an influence of short-term solar activity variations on mesopause region airglow?" In: *Advances in Space Research* 39.8, pp. 1248–1255. DOI: 10.1016/j.asr.2007.01.002.

Schlegel, K., A. Brekke, and A. Haug (1978). "Some characteristics of the quiet polar D-region and mesosphere obtained with the partial reflection method". In: *Journal of Atmospheric and Terrestrial Physics* 40.2, pp. 205–213. DOI: 10.1016/0021-9169(78)90025-9.

Schmidt, H., G. P. Brasseur, M. Charron, E. Manzini, M. A. Giorgetta, T. Diehl, V. I. Fomichev, D. Kinnison, D. Marsh, and S. Walters (2006). "The HAMMONIA chemistry climate model: Sensitivity of the mesopause region to the 11-year solar cycle and CO_2 doubling". In: *Journal of Climate* 19.16, pp. 3903–3931. DOI: 10.1175/JCLI3829.1.

Schoeberl, M. R. and D. L. Hartmann (1991). "The dynamics of the stratospheric polar vortex and its relation to springtime ozone depletions". In: *Science* 251, pp. 46–52. DOI: 10.1126/science.251.4989.46.

She, C. Y. and D. A. Krueger (2004). "Impact of natural variability in the 11-year mesopause region temperature observation over Fort Collins, CO (41°N, 105°W)". In: *Advances in Space Research* 34.2, pp. 330–336. DOI: 10.1016/j.asr.2003.02.047.

Shepherd, G. G., G. Liu, and R. G. Roble (2005). "Large-scale circulation of atomic oxygen in the upper mesosphere and lower thermosphere". In: *Advances in Space Research* 35, pp. 1945–1950. DOI: 10.1016/j.asr.2004.12.036.

Shepherd, M. G., P. J. Espy, C. Y. She, W. Hocking, P. Keckhut, G. Gavrilyeva, G. G. Shepherd, and B. Naujokat (2002). "Springtime transition in upper mesospheric temperature in the northern hemisphere". In: *Journal of Atmospheric and Solar-Terrestrial Physics* 64.8, pp. 1183–1199. DOI: 10.1016/S1364-6826(02)00068-8.

Shine, K. P. (1987). "The middle atmosphere in the absence of dynamical heat fluxes". In: *Quarterly Journal of the Royal Meteorological Society* 113.476, pp. 603–633. DOI: 10.1002/qj.49711347610.

Shiotani, M. and I. Hirota (1985). "Planetary wave-mean flow interaction in the stratosphere: A comparison between northern and southern hemispheres". In: *Quarterly Journal of the Royal Meteorological Society* 111.468, pp. 309–334. DOI: 10.1002/qj.49711146804.

Sigernes, F., N. Shumilov, C. S. Deehr, K. P. Nielsen, T. Svenøe, and O. Havnes (2003). "Hydroxyl rotational temperature record from the auroral station in Adventdalen, Svalbard $78°N, 15°E$)". In: *Journal of Geophysical Research: Space Physics* 108.A9. DOI: 10.1029/2001JA009023.

Singer, W., P. Hoffmann, A. H. Manson, C. E. Meek, R. Schminder, D. Kürschner, G. A. Kokin, A. K. Knyazev, Y. I. Portnyagin, N. A. Makarov, A. N. Fakhrutdinova, V. V. Sidorov, G. Cevolani, H. G. Muller, E. S. Kazimirovsky, V. A. Gaidukov, R. R. Clark, R. P. Chebotarev, and Y. Karadjaev (1994). "The wind regime of the mesosphere and lower thermosphere during the DYANA campaign—I. Prevailing winds". In: *Journal of Atmospheric and Terrestrial Physics* 56.13-14, pp. 1717–1729. DOI: 10.1016/0021-9169(94)90006-X.

Sivjee, G. G. (1992). "Airglow hydroxyl emissions". In: *Planetary and Space Science* 40.2-3, pp. 235–242. DOI: 10.1016/0032-0633(92)90061-R.

Sivjee, G. G. and R. M. Hamwey (1987). "Temperature and chemistry of the polar mesopause OH". In: *Journal of Geophysical Research: Space Physics* 92.A5, pp. 4663–4672. DOI: 10.1029/JA092iA05p04663.

Sivjee, G. G., R. L. Walterscheid, J. H. Hecht, R. M. Hamwey, G. Schubert, and A. B. Christensen (1987). "Effects of atmospheric disturbances on polar mesopause airglow OH emissions". In: *Journal of Geophysical Research: Space Physics* 92.A7, pp. 7651–7656. DOI: 10.1029/JA092iA07p07651.

Stray, N. H., R. J. de Wit, P. J. Espy, and R. E. Hibbins (2014). "Observational evidence for temporary planetary wave forcing of the MLT during fall equinox". In: *Geophysical Research Letters* 41.17, pp. 6281–6288. DOI: 10.1002/2014GL061119.

Thomas, R. J., C. A. Barth, G. J. Rottman, D. W. Rusch, G. H. Mount, G. M. Lawrence, R. W. Sanders, G. E. Thomas, and L. E. Clemens (1983). "Mesospheric ozone depletion during the solar proton event of July 13, 1982. Part I Measurement". In: *Geophysical Research Letters* 10.4, pp. 253–255. DOI: 10.1029/GL010i004p00253.

Tiao, G. C., G. C. Reinsel, D. Xu, J. H. Pedrick, X. Zhu, A. J. Miller, J. J. DeLuisi, C. L. Mateer, and D. J. Wuebbles (1990). "Effects of autocorrelation and temporal sampling schemes on estimates of trend and spatial correlation". In: *Journal of Geophysical Research: Atmospheres* 95.D12, pp. 20507–20517. DOI: 10.1029/JD095iD12p20507.

Turnbull, D. N. and R. P. Lowe (1989). "New hydroxyl transition probabilities and their importance in airglow studies". In: *Planetary and Space Science* 37.6, pp. 723–738. DOI: 10.1016/0032-0633(89)90042-1.

Viereck, R. A. and C. S. Deehr (1989). "On the interaction between gravity waves and the OH Meinel (6-2) and the O_2 atmospheric (0-1) bands in the polar night airglow". In: *Journal of Geophysical Research: Space Physics* 94.A5, pp. 5397–5404. DOI: 10.1029/JA094iA05p05397.

Von Savigny, C., I. C. McDade, K.-U. Eichmann, and J. P. Burrows (2012). "On the dependence of the OH* Meinel emission altitude on vibrational level: SCIAMACHY observations and model simulations". In: *Atmospheric Chemistry and Physics* 12.18, pp. 8813–8828. DOI: 10.5194/acp-12-8813-2012.

Walterscheid, R. L., G. G. Sivjee, and R. G. Roble (2000). "Mesospheric and lower thermospheric manifestations of a stratospheric warming event over Eureka, Canada (80°N)". In: *Geophysical Research Letters* 27.18, pp. 2897–2900. DOI: 10.1029/2000GL003768.

Walterscheid, R. L., G. G. Sivjee, G. Schubert, and R. M. Hamwey (1986). "Large-amplitude semidiurnal temperature variations in the polar mesopause: evidence of a pseudotide". In: *Nature* 324.6095, pp. 347–349. DOI: 10.1038/324347a0.

Warhaft, Zellman (1997). *An introduction to thermal-fluid engineering: The engine and the atmosphere*. Cambridge University Press.

Waters, J. W., L. Froidevaux, R. S. Harwood, R. F. Jarnot, H. M. Pickett, W. G. Read, P. H. Siegel, R. E. Cofield, M. J. Filipiak, D. A. Flower, et al. (2006). "The earth observing system microwave limb sounder (EOS MLS) on the Aura satellite". In: *IEEE Transactions on Geoscience and Remote Sensing* 44.5, pp. 1075–1092. DOI: 10.1109/TGRS.2006.873771.

Weatherhead, E. C., G. C. Reinsel, G. C. Tiao, X.-L. Meng, D. Choi, W.-K. Cheang, T. Keller, J. DeLuisi, D. J. Wuebbles, J. B. Kerr, A. J. Miller, S. J. Oltmans, and J. E. Frederick (1998). "Factors affecting the detection of trends: Statistical considerations and applications to environmental data".

In: *Journal of Geophysical Research* 103.D14, pp. 17–149. DOI: 10.1029/98JD00995.

Weinstock, J. (1978). "Vertical turbulent diffusion in a stably stratified fluid". In: *Journal of the Atmospheric Sciences* 35.6, pp. 1022–1027. DOI: 10.1175/1520-0469(1978)035<1022:VTDIAS>2.0.CO;2.

Yee, J.-H., G. Crowley, R. G. Roble, W. R. Skinner, M. D. Burrage, and P. B. Hays (1997). "Global simulations and observations of $O(^1S)$, $O_2(^1\Sigma)$ and OH mesospheric nightglow emissions". In: *Journal of Geophysical Research* 102.A9, pp. 19949–19968. DOI: 10.1029/96JA01833.

Younger, J. P., C. S. Lee, I. M. Reid, R. A. Vincent, Y. H. Kim, and D. J. Murphy (2014). "The effects of deionization processes on meteor radar diffusion coefficients below 90 km". In: *Journal of Geophysical Research: Atmospheres* 119.16, pp. 10027–10043. DOI: 10.1002/2014JD021787.

A. Appendix

Figure A.1.: Map of part of the Arctic. Longyearbyen and Tromsø are marked in red. Image courtesy: Google Maps.

Figure A.2.: Map of Longyearbyen and surrounding areas. The locations of the old auroral station and the Kjell Henriksen Observatory are marked as black and red stars. Image courtesy: TopoSvalbard, Norwegian Polar Institute.

Figure A.3.: Map of Tromsø and surrounding areas. The location of Ramfjordmoen research station is marked as a black and red star. Image courtesy: Norgeskart, Norwegian Mapping Authority.

B. Papers